Study of Nuclear Reactions with ^{11}C and ^{15}O Radioactive Ion Beams

By

Dongwon Lee

B.S. (Seoul National University) 1999
M.S. (Seoul National University) 2001

A dissertation submitted in partial satisfaction of the

Requirements for the degree of

Doctor of Philosophy

in

Engineering – Nuclear Engineering

in the

Graduate Division

of the

University of California, Berkeley

Committee in charge:

Professor Joseph Cerny, Co-chair

Professor Jasmina Vujic, Co-chair

Professor Edward Morse

Professor Heino Nitsche

Spring 2007

Abstract

Study of Nuclear Reactions with ^{11}C and ^{15}O Radioactive Ion Beams

By

Dongwon Lee

Doctor of Philosophy in Engineering – Nuclear Engineering

University of California, Berkeley

Professor Joseph Cerny, Co-chair

Professor Jasmina Vujic, Co-chair

Nuclear reaction study with radioactive ion beams is one of the most exciting research topics in modern nuclear physics. The development of radioactive ion beams has allowed nuclear scientists and engineers to explore many unknown exotic nuclei far from the valley of nuclear stability, and to further our understanding of the evolution of the universe.

The recently developed radioactive ion beam facility at the Lawrence Berkeley National Laboratory's 88-inch cyclotron is denoted as BEARS and provides ^{11}C, ^{14}O and ^{15}O radioactive ion beams of high quality. These moderate to high intensity, proton-rich radioactive ion beams have been used to explore the properties of unstable nuclei such as ^{12}N and ^{15}F.

In this work, the proton capture reaction on ^{11}C has been evaluated via the indirect $d(^{11}C,^{12}N)n$ transfer reaction using the inverse kinematics method coupled with the

Asymptotic Normalization Coefficient (ANC) theoretical approach. The total effective $^{12}N\rightarrow^{11}C+p$ ANC is found to be $\left(C_{eff}^{^{12}N}\right)^2 = 1.83 \pm 0.27\,fm^{-1}$. With the high ^{11}C beam intensity available, our experiment showed excellent agreement with theoretical predictions and previous experimental studies. This study also indirectly confirmed that the $^{11}C(p,\gamma)$ reaction is a key step in producing CNO nuclei in supermassive low-metallicity stars, bypassing the slow triple alpha process.

The newly developed ^{15}O radioactive ion beam at BEARS was used to study the poorly known level widths of ^{16}F via the $p(^{15}O,^{15}O)p$ reaction. Among the nuclei in the A=16, T=1 isobaric triad, many states in ^{16}N and ^{16}O have been well established, but less has been reported on ^{16}F. Four states of ^{16}F below 1 MeV have been identified experimentally: 0^-, 1^-, 2^-, and 3^- (E_x = 0.0, 0.19, 0.42, and 0.72 MeV, respectively). Our study utilized R-matrix analysis and found that the 0^- state has a level width of 23.1 ± 2.2 keV, and that the broader 1^- state has a width of 91.1 ± 9.9 keV. The level width of the 2^- state is found to be 3.3 ± 0.6 keV which is much narrower than the compiled value of 40 ± 30 keV, while a width of 14.1 ± 1.7 keV for the 3^- state is in good agreement with the reported value (< 15 keV). These experimental level widths of all four levels are also in accordance with theoretical predictions using single particle shell model calculation.

To my late father, and my family members

Table of Contents

CHAPTER 1. Introduction

CHAPTER 2. Radioactive Ion Beams

CHAPTER 3. Nuclear Reactions in Stars

CHAPTER 4. Nuclear Reaction Theory

CHAPTER 5. Study of the ^{11}C(p,γ) Reaction via the Indirect d(^{11}C,^{12}N)n Transfer Reacton

CHAPTER 6. Study of Low-lying Resonant States in ^{16}F using an ^{15}O Radioactive Ion Beam

CHAPTER 7. Conclusion

References

List of Figures

List of Tables

Acknowledgments

CHAPTER 1
Introduction

1.1 The Landscape of Exotic Nuclei

The origin of the universe has been one of the unexplained mysteries in modern science. Nuclei are made from cataclysmic events in the evolution of the universe. Although light nuclei were created within a few minutes after the Big Bang, heavier nuclei were produced, and are still being made, from nucleosynthesis in stars. In order to understand the fundamentals and origin of the physical world in which we live, it is necessary for us to understand the properties of nuclei. Our knowledge of nuclei has been founded mostly from intensive studies of stable nuclei on earth. However, almost every stellar process involves unstable nuclei. Therefore, a full understanding of unstable nuclei is indispensable for us to fully answer the origin of life forms, the materials surrounding us, and finally, the origin of the universe.

Nuclei are composed of protons and neutrons, and come in a variety of combinations of protons and neutrons. Figure 1.1 (taken from Ref. [Ca97]) is known as the nuclear landscape, showing all the stable nuclei plus the known radioactive nuclei, as well as unknown territory, "Terra Incognita". This figure shows approximately six thousand nuclei that are expected to exist by the strong force. The number of stable nuclei forming the valley of stability is less than 300. About 2200 of the known nuclei are radioactive while another 3500 nuclei are still unexplored. Hence, to fully understand nuclei, we need

to study those that reside very far from the stable isotopes toward the limits of nuclear stability.

The proton drip line lies much closer to the valley of stability because of the existence of the repulsive Coulomb force between the protons in the nucleus and the core. In this region, proton radioactivity and the nuclear structure of proton-rich nuclei become of great interest. In contrast, the neutron drip line is considerably further from the valley of stability and harder to approach. In addition, the exploration of superheavy elements above the atomic number of 110 remains a major challenge to nuclear physics and nuclear chemistry.

Nuclei play a critical role in astrophysical processes. Light nuclei such as carbon and oxygen are made from stellar evolution while elements heavier than iron are created in explosive stellar events. Unstable nuclei become very important links in a chain of nucleosynthesis, producing heavier elements by capturing protons or neutrons. The synthesis of nuclei in violent stellar events depends sensitively on the properties of unstable nuclei. Therefore, the experimental study of these astrophysical processes requires measurements of reactions involving short-lived radioactive species. Figure 1.2 [Ca97] shows many interesting research topics in different regions of the nuclear landscape in terms of nuclear astrophysics.

The advent of radioactive ion beams has opened a new era of nuclear physics, and many research opportunities are being investigated with these beams. Several examples of interesting research topics are shown in Table 1.1 [Ca97]. There is no doubt that radioactive ion beams have become indispensable tools for studies in modern nuclear

physics. The availability of radioactive beams allows us to explore the unknown territory of the nuclear landscape beyond the current limits, extending our horizons substantially.

This thesis will utilize the Berkeley Experiments with Accelerated Radioactive Species (BEARS) facility at the 88-inch cyclotron at the Lawrence Berkeley National Laboratory (LBNL) to study the reaction properties of proton rich light nuclei using beams of ^{11}C and ^{15}O radioactive isotopes. It describes the efforts to examine two interesting nuclear reactions involving proton rich radioactive ion beams: the experimental studies of the ^{11}C(p,γ) proton capture reaction strength via the alternate d(^{11}C,^{12}N)n transfer reaction, and the low lying level structure of ^{16}F through ^{15}O+p elastic resonance scattering in inverse kinematics.

1.2 Thesis Organization

Following this introduction, Chapter 2 presents a brief overview of radioactive ion beams, including the production methods in use. The importance of radioactive ion beams in modern nuclear physics and nuclear astrophysics will also be discussed. In addition, the BEARS radioactive ion beam facility at LBNL will be presented. Chapter 3 is dedicated to the basic astrophysical processes from the viewpoint of nuclear reactions. This chapter mainly deals with stellar processes involving light nuclei. Hydrogen burning processes such as the pp-chain and the CNO cycle are introduced. Furthermore, the helium burning process is discussed briefly. Basic concepts of the astrophysical S-factor and stellar reaction rates are quantitatively explained. This chapter will provide a basic understanding of energy production in many stars, including our Sun.

Nuclear reaction research with unstable nuclei needs fundamental analysis tools to convert experimental data into meaningful results. Elastic resonance scattering is one of the most useful methods to explore the level structures of unknown or poorly known nuclei, especially when this technique is combined with thick target inverse kinematics. This technique with radioactive ion beams allowed us to reveal unknown spectroscopic information on several proton-rich nuclei, e.g., ^{12}N via ^{11}C+p [Pe06], and ^{15}F via ^{14}O+p reactions [Gu04, Gu05]. In order to compare experimental results with theoretical predictions, R-matrix theory (or resonance scattering theory) is necessary. The first part of Chapter 4 introduces this R-matrix theory quantitatively.

Nuclear astrophysics is opening up as a more vigorous research field, and many important nuclear reactions involving unstable nuclei have yet to be studied. Difficulties inherent in these experiments include the fact that we are unable to reproduce stellar environments in the laboratory. For example, the cross section for the ^{11}C(p,γ) capture reaction is very important, but it is so small that direct measurements are essentially impossible with currently available beam intensities. However, an indirect measurement with the d(^{11}C,^{12}N)n reaction allows us to deduce the reaction rate of ^{11}C(p,γ) in stellar environments. This approach is known as the Asymptotic Normalization Coefficient (ANC) method, and has turned out to be a very useful and reliable tool for analyzing proton capture reactions. The theoretical background of the ANC method is also presented in Chapter 4.

The BEARS facility at the 88-inch cyclotron provides high quality radioactive ion beams such as ^{11}C ($T_{1/2}$ = 20 min), ^{14}O ($T_{1/2}$ = 71 sec), and ^{15}O ($T_{1/2}$ = 122 sec). The availability of these nuclear beams allowed us to explore several proton rich nuclei of

interest. Although the ^{11}C(p,γ) reaction is recognized as one of the key reactions in the evolution of supermassive stars, its reaction rate has been only estimated theoretically due to the lack of experimental information. Recently, a few studies have provided experimental reaction rates using a ^{11}C beam and the ANC method. Our d(^{11}C,^{12}N)n experiment with BEARS successfully confirmed these new results, and the details are presented in Chapter 5.

This thesis also exploits the newly developed ^{15}O beam from BEARS to study the low lying structure of ^{16}F. The level widths of the first four states in ^{16}F (all proton unbound) have remained uncertain while those of its mirror nuclide ^{16}N were well established. Elastic resonance scattering of ^{15}O+p is reported for the first time, and is presented in Chapter 6 in detail. Finally, my conclusions and other research opportunities with BEARS radioactive ion beams will be discussed in Chapter 7.
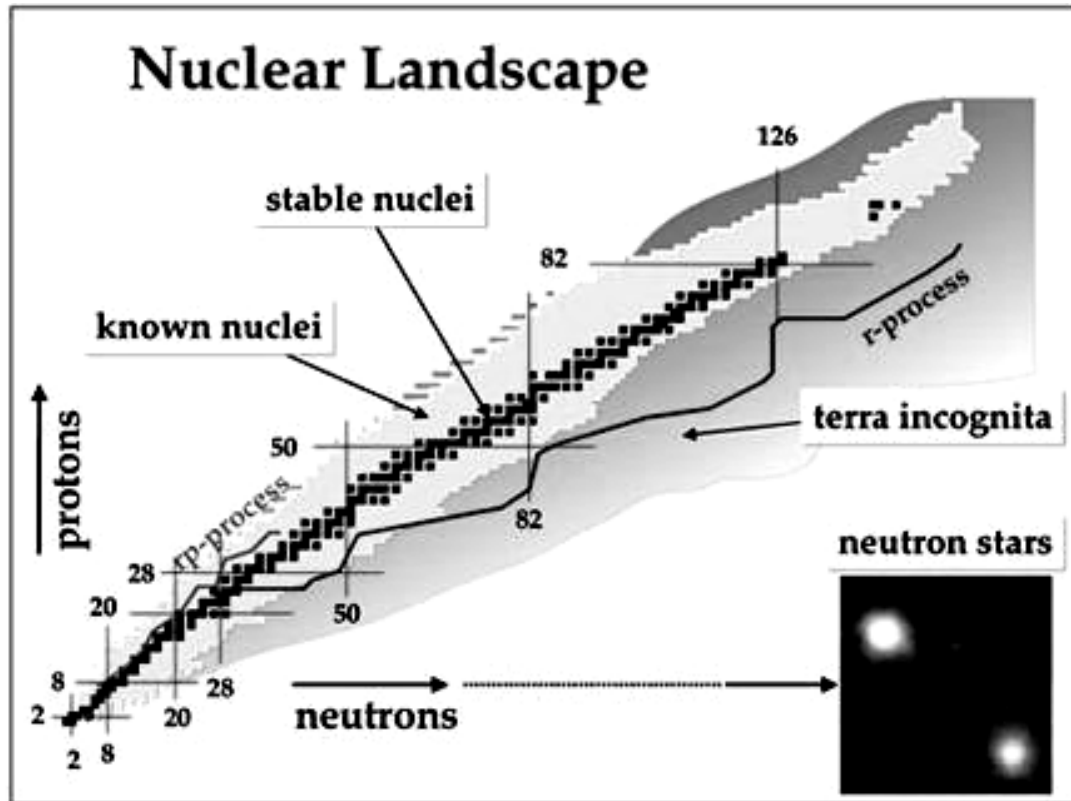
Figure 1.1 The nuclear landscape showing the known nuclei and terra incognita. The black squares represent the stable nuclei. The adjacent region shows known short-lived unstable nuclei. Terra incognita comprises those nuclei which are still unexplored.
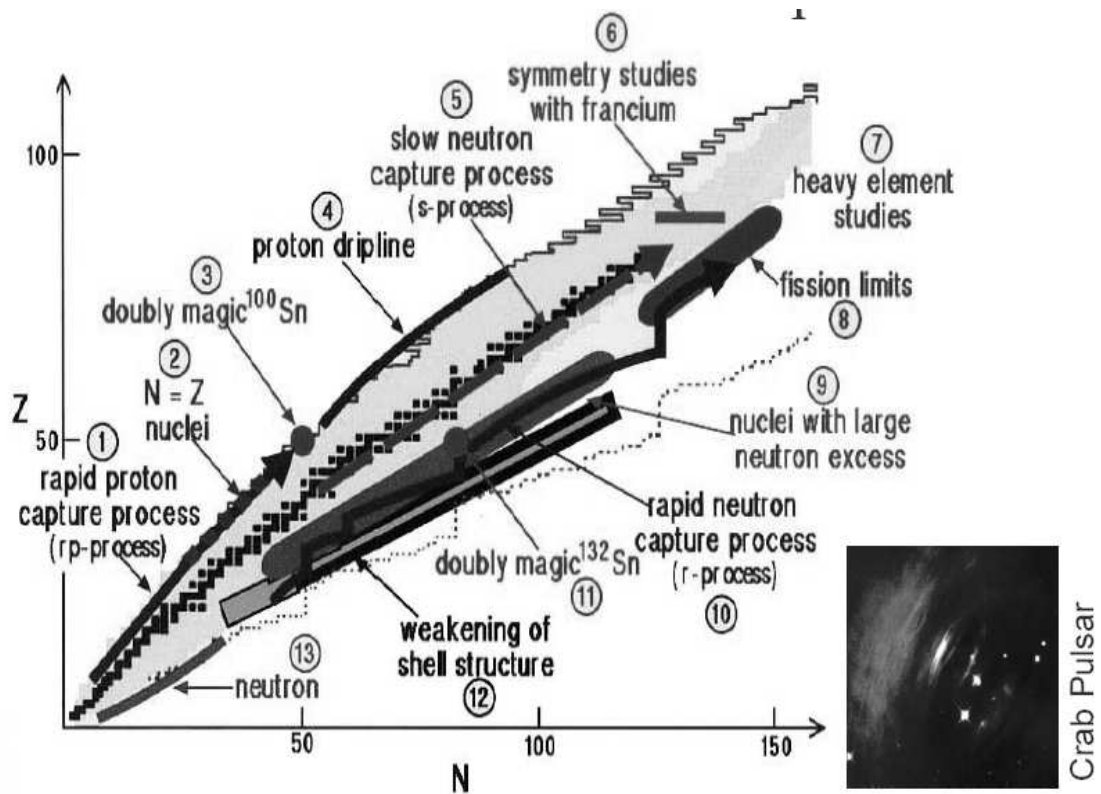
Figure 1.2 Astrophysics on the nuclear landscape. Many interesting astrophysical processes are shown in different regions of the nuclear landscape (these topics are explained in the Table 1.1)

Table 1.1 Representative examples of research topics with radioactive ion beams [Ca97].

Physics topics	Reactions and Techniques	Beams	Desired Intensities [particles/sec]	Energy Range [MeV/nucleon]
1. Rapid proton capture (rp processes)	Transfer, elastic, inelastic, radiative capture, Coulomb dissociation	^{14}O, ^{15}O, ^{26}Si, ^{34}Ar, ^{56}Ni	10^8-10^{11} 10^5-10^{11}	0.15-15
2. Reactions with and studies of N=Z nuclei, symmetry studies	Transfer, fusion, decay studies	^{56}Ni, ^{62}Ga, ^{64}Ge, ^{68}Ge, ^{67}As, ^{72}Kr	10^4-10^9	0.1-15
3. Decay studies of ^{100}Sn	Decay	^{100}Sn	1-10	low energy
4. Proton drip line studies	Decay, fusion, transfer	^{56}Ni, ^{64,66}Ge, ^{72}Kr	10^6-10^9	5
5. Slow neutron capture(s-process)	Capture	^{134,135}Cs, ^{155}Eu	10^8-10^{11}	0.1
6. Symmetry studies with francium	Decays, traps	Fr	10^{11}	low energy
7. Heavy element studies	Fusion, decay	$^{50-52}$Ca, ^{72}Ni, ^{84}Ge, ^{96}Kr	10^4-10^7 10^6-10^8	5-8
8. Fission limits	Fusion-fission	$^{140-144}$Xe, $^{142-146}$Cs, ^{142}I, $^{145-148}$Xe, $^{147-150}$Cs	10^7-10^{11} 10^4-10^7	5
9. Rapid neutron capture(r-process)	Capture, decay, mass measurement	^{130}Cd, ^{132}Sn, ^{142}I	10^4-10^9	0.1-5
10. Nuclei with large neutron excess	Fusion, transfer, deep inelastic	$^{140-144}$Xe, $^{142-146}$Cs, ^{142}I, $^{145-148}$Xe, $^{147-150}$Cs	10^7-10^{11} 10^2-10^7	5-15
11. Single-particle states / effective nucleon-nucleon interactions	Direct reactions, nucleon transfer	^{132}Sn, ^{133}Sb	10^8-10^9	5-15
12. Shell structure, weakening of gaps, spin-orbit potential	Mass measurement, Coulomb excitation, fusion, nucleon transfer, deep inelastic	Kr, Sn, Xe	10^2-10^9	0.1-10
13. Neutron-drip line studies, halo nuclei	Mass measurement, nucleon transfer	^{8}He, ^{11}Li, ^{29}Ne , ^{31}Na, ^{76}Cu	10^6-10^8 10^3-10^6	5-10

CHAPTER 2
Radioactive Ion Beams

2.1 Introduction

The study of exotic nuclei is currently one of the most exciting research fields in modern nuclear physics because the structure and decay modes of many nuclei far from stability are still unknown. The nuclear properties of these radioactive species are of major interest to experimentalists at many research facilities over the world. We now know that the nuclear structures and properties of nuclei toward the proton or neutron drip lines can be quite unusual and so provide challenges to our traditional knowledge obtained from experiences with nuclei at or near stability.

For proton-rich nuclei, the proton drip line is much closer to the valley of stability so that this drip line has been established for many elements up to and even somewhat beyond lead [Ro98]. Hence, short-lived, proton-rich radioactive beams will allow scientists to study nuclear levels and structures of proton-rich nuclei in the vicinity of the proton drip line as well as their astrophysical consequences.

The development of radioactive ion beams using a variety of techniques has allowed many nuclear reactions of exotic nuclei to be studied for the first time. This strong interest in accelerated radioactive ion beams is reflected in the many worldwide facilities that are in operation, under construction or being proposed. The radioactive ion beam facilities worldwide are shown in Figure 2.1, taken from Ref. [Da05]. A brief review of

radioactive ion beam production methods and their characteristics are discussed, and the BEARS system at LBNL is introduced in this chapter.

2.2 Production Methods of Radioactive Ion Beams

Many radioactive ion beam facilities are based either on in-flight Projectile Fragmentation (PF) or on Isotope Separation On-Line (ISOL) methods. Projectile Fragmentation was pioneered in the beginning of the 1980's. An energetic ion beam is fragmented, passing through a thin target, and a highly selected reaction product is transported to a secondary target. During transit, mass, charge and momentum selection are necessary. In the PF method, high-energy stable beams (from several tens to several hundreds of MeV per nucleon) are used. The reaction products are emitted in the forward direction with about the same velocity as the primary beam so that no post-acceleration is needed. This method is illustrated in Figure 2.2 (top) [Ca97].

In the ISOL method which mainly utilizes two accelerators [Ve96, Ca97], the radioactive nuclei are produced in a thick target by particles from a primary beam or driver accelerator. These are extracted from the target and transferred to an ion source. Ionized radioactive nuclides are then fed into a second accelerator to provide the radioactive beam. A wide range of primary beams including thermal neutrons, medium energy deuterons, high energy protons, and intermediate energy heavy ions are in use. This method is illustrated in Figure 2.2 (bottom) [Ca97].

The ISOL technique allows the radioactive beams to be delivered with high quality and readily variable beam energy, which are suitable for nuclear structure and nuclear

astrophysics studies. However, a time delay and intensity loss resulting from the stopping and extraction from the target is a drawback of the ISOL method. The PF method delivers radioactive beams with a time delay typically only of microseconds. Both methods require effort to reduce contamination from other components in the beam delivered on the secondary target. It should also be noted that a hybrid arrangement capable of ion beam production by both methods has been proposed in the original Rare Isotope Accelerator (RIA) concept as shown in Figure 2.3 [Ri06].

2.3 BEARS Overview

The BEARS system is a unique radioactive ion beam facility, which was developed based on the ISOL method at LBNL [Ce96, Ce99]. BEARS utilizes two existing accelerators to produce radioactive species and provide accelerated beams to the experimental areas at the 88-inch cyclotron. BEARS has provided proton-rich radioactive ion beams of ^{11}C, ^{14}O, and ^{15}O. Production of the ^{11}C/^{14}O/^{15}O beam begins at LBNL's biomedical isotope facility (BIF), using a 40 μA, 10 MeV proton beam bombarding a high-pressure nitrogen gas target. Both ^{14}O ($T_{1/2}$ = 71 sec) and ^{11}C ($T_{1/2}$ = 20 min) are produced in the same nitrogen target, through the ^{14}N(p,n) and ^{14}N(p,α) reactions, respectively. For the case of ^{15}O ($T_{1/2}$ = 122 sec), a ^{15}N gas target is used. Target system produces ^{11}C as a form of carbon dioxide and releases it to go down the line. BIF is located about 350 m from the 88-Inch Cyclotron, and activity is rapidly transported as carbon dioxide, pushed by a flow of helium through an evacuated capillary tube that connects the two buildings. At the 88-Inch Cyclotron, the carbon dioxide is cryogenically separated from the bulk of the carrier helium, before being injected into the Advanced

Electron Cyclotron Resonance (AECR) ion source for subsequent ionization and acceleration [Jo00, Po00, Po03, Po05]. Figure 2.4 shows the transfer line, connecting BIF and the 88-inch Cyclotron.

The BIF gas target system is filled with nitrogen target gas. The target is first partially loaded with 1% O_2 plus 99% N_2 to 4.4 atm, then topped off to 22 atm with pure nitrogen. The gas is then bombarded with 10 MeV protons for a fixed time. Then, the beam is shut off and the irradiated gas is unloaded into a holding tank, where the $^{11}CO_2$ gas is held prior to transport. After unloading, the target is refilled and the cycle is repeated. In order to be transported and cryogenically separated by the rest of the BEARS system, the ^{11}C activity must take the chemical form of CO_2 [Po00].

For the case of ^{14}O, additional conversion steps are necessary. A mixture of a few percent hydrogen is added to the nitrogen, which is then used to capture ^{14}O in the form of water, $H_2{}^{14}O$. However, water is not a good chemical form for use with BEARS, since it can stick in the long unheated transport line. To overcome this problem, an automated system was constructed to convert the water to carbon dioxide. First, the target is unloaded and the water is temporarily frozen in a small coil of stainless steel tubing, cooled to - 40 °C by a stream of cold dry air from a vortex tube. This allows the elimination of the other target gas components, producing a clean sample of $H_2{}^{14}O$. The ^{14}O water is released through a momentary resistive heating of the steel trapping coil with a strong electric current. A flow of helium carries the activity through a small tube furnace containing carbon granules at high temperatures (1,000 ~ 1,100 °C). This converts the water vapor to carbon monoxide ($H_2{}^{14}O$ + carbon $\rightarrow$ C^{14}O + H_2). The carbon monoxide is then oxidized to carbon dioxide over a platinum catalyst at 180 °C. The

resulting $[^{14}O]CO_2$ is then in a chemical form used by the existing BEARS system. The complete trapping and conversion process takes about 10 seconds, and the conversion efficiency is better than 50% [Po03]. The overall process including transport to the AECR ion source takes about one ^{14}O half-life. Production of ^{15}O goes through the same processes as ^{14}O, but the unloaded ^{15}N target gas is recycled to be re-injected into the target chamber [Po06]. This conversion system for ^{14}O is shown in Figure 2.5.

The transport system carries the activity from the BIF facility to the 88-inch cyclotron. To transport the gas, pressurized helium gas drives the target gas down the evacuated transport capillary. Transport between the two buildings takes about 12 seconds. All the activity arrives at the 88-inch Cyclotron within a spike of about 2 seconds. The gas flow is then diverted through the cryogenic trap. The cryogenic trap, a stainless steel coil submerged in liquid nitrogen, captures the $^{11}CO_2$ or $[^{14,15}O]CO_2$ and any remaining nitrogen gas is removed. The diagram of the BEARS transport system is shown in Figure 2.6.

Before being injected into the AECR-U ion source, the $^{11}C/^{14}O/^{15}O$ activity must be released from the cryogenic trap by heating. After most of the helium drive gas has been pumped away, warming of the trap is begun. When the temperature of the trap reaches 120 K, the trap is connected to a reservoir, which is located as close to the ion source as possible. As the trap continues to warm, $^{11}C/^{14}O/^{15}O$ activity, believed to still be in the form of CO_2, is released from the trap and passes into the reservoir. The gas in the reservoir is bled into the ion source at a controlled flow rate because the controlled injection of activity is crucial to achieve stable operation of the AECR-U ion source. The $^{11}C/^{14}O/^{15}O$ is then ionized, extracted, and accelerated by the 88-inch cyclotron and

transported to an experimental area. In this thesis, the ^{11}C beam was transported to Cave 4A and the ^{15}O beam was transported to Cave 0-2.
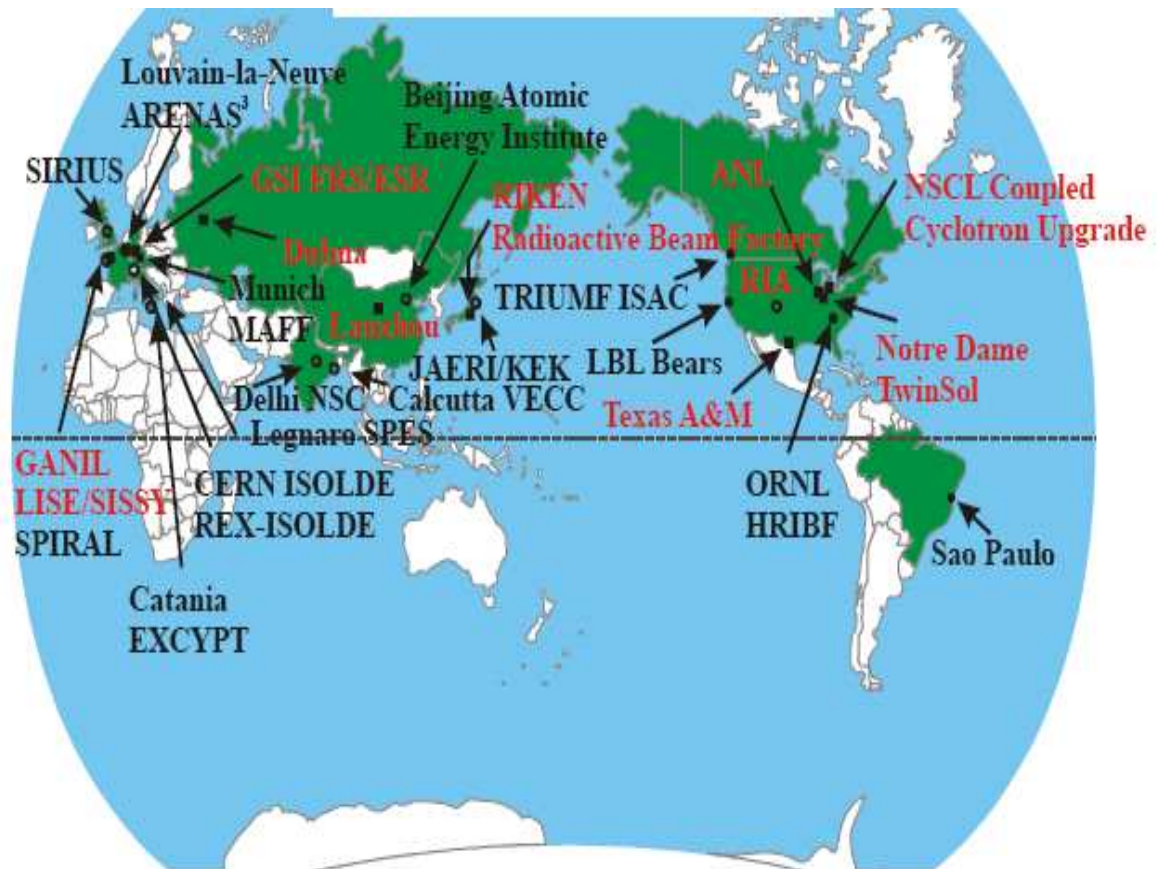
Figure 2.1 Radioactive ion beam facilities around the world.
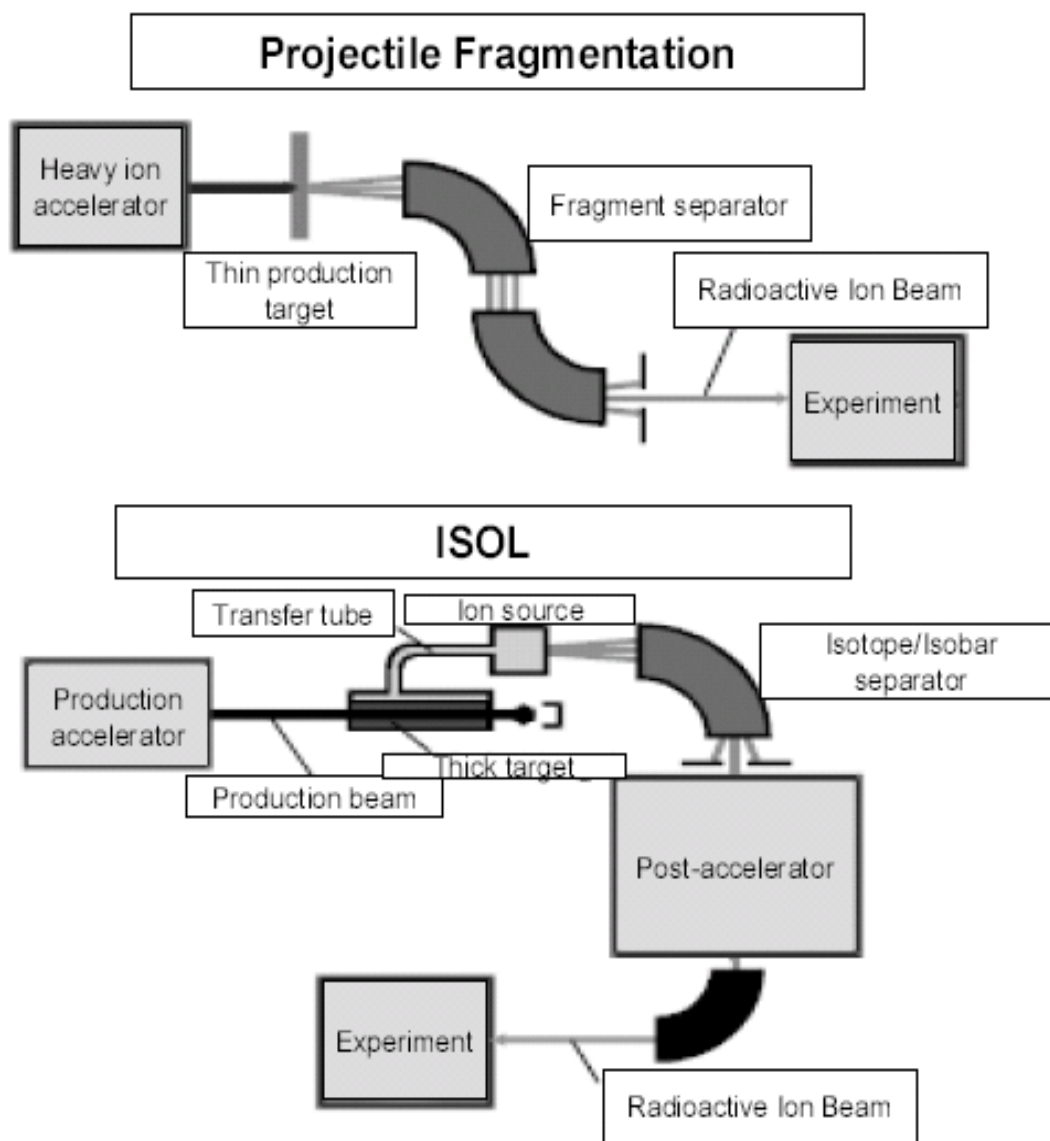
Figure 2.2 Schematic diagrams of the two radioactive ion beam production methods in use.
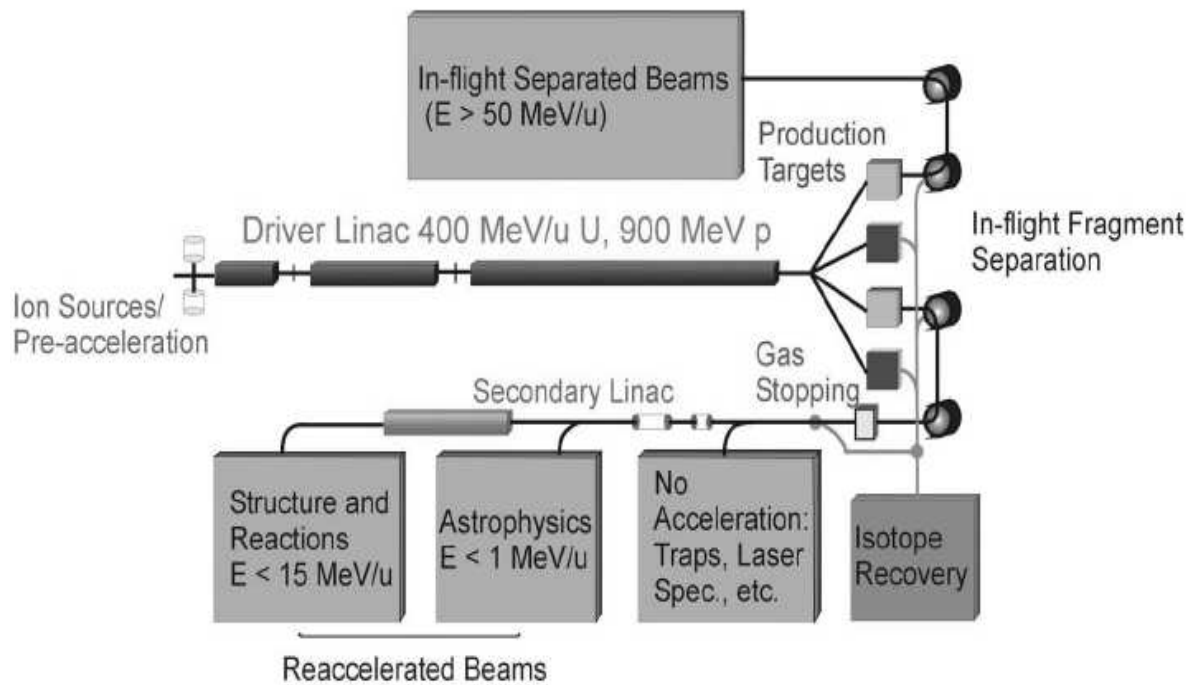
Figure 2.3 Proposed hybrid method for the Rare Isotope Accelerator (RIA) in the US.
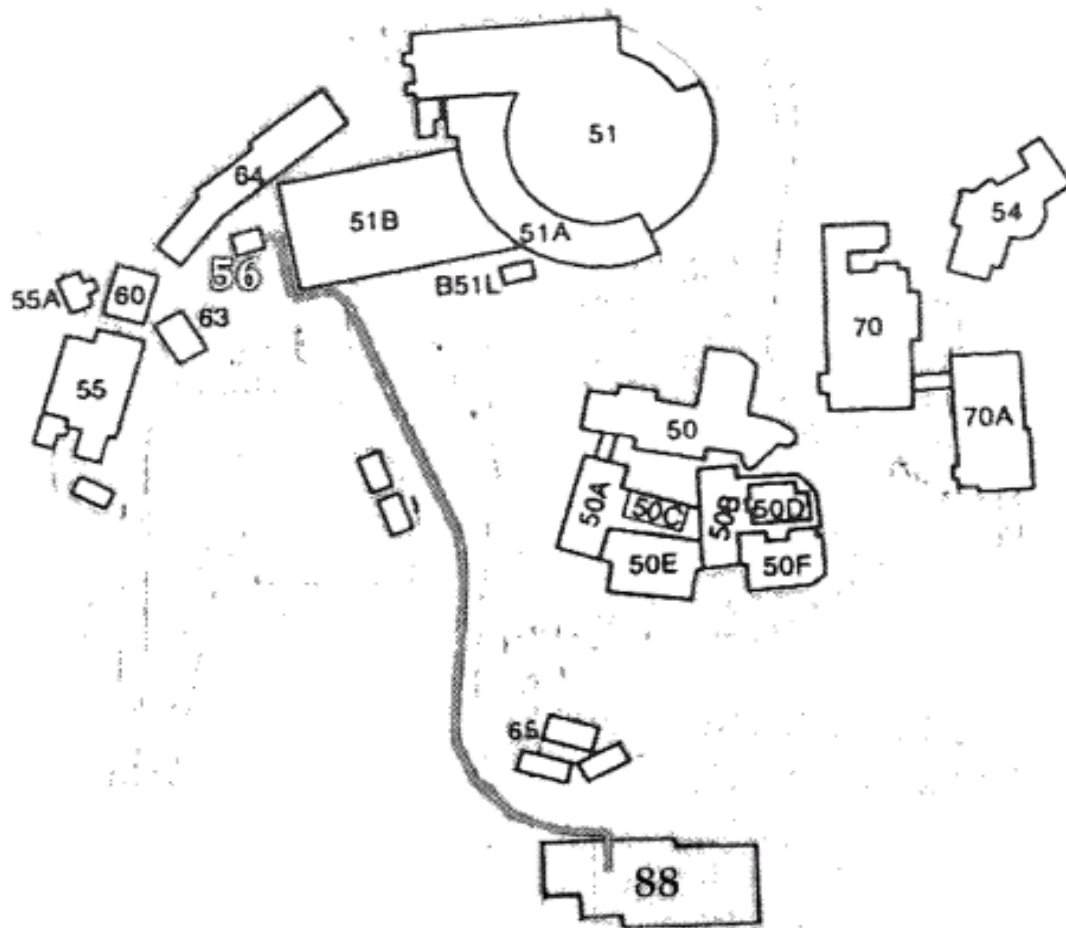
Figure 2.4 The transfer line between BIF (Bldg. 56) and the 88-inch Cyclotron (Bldg. 88).
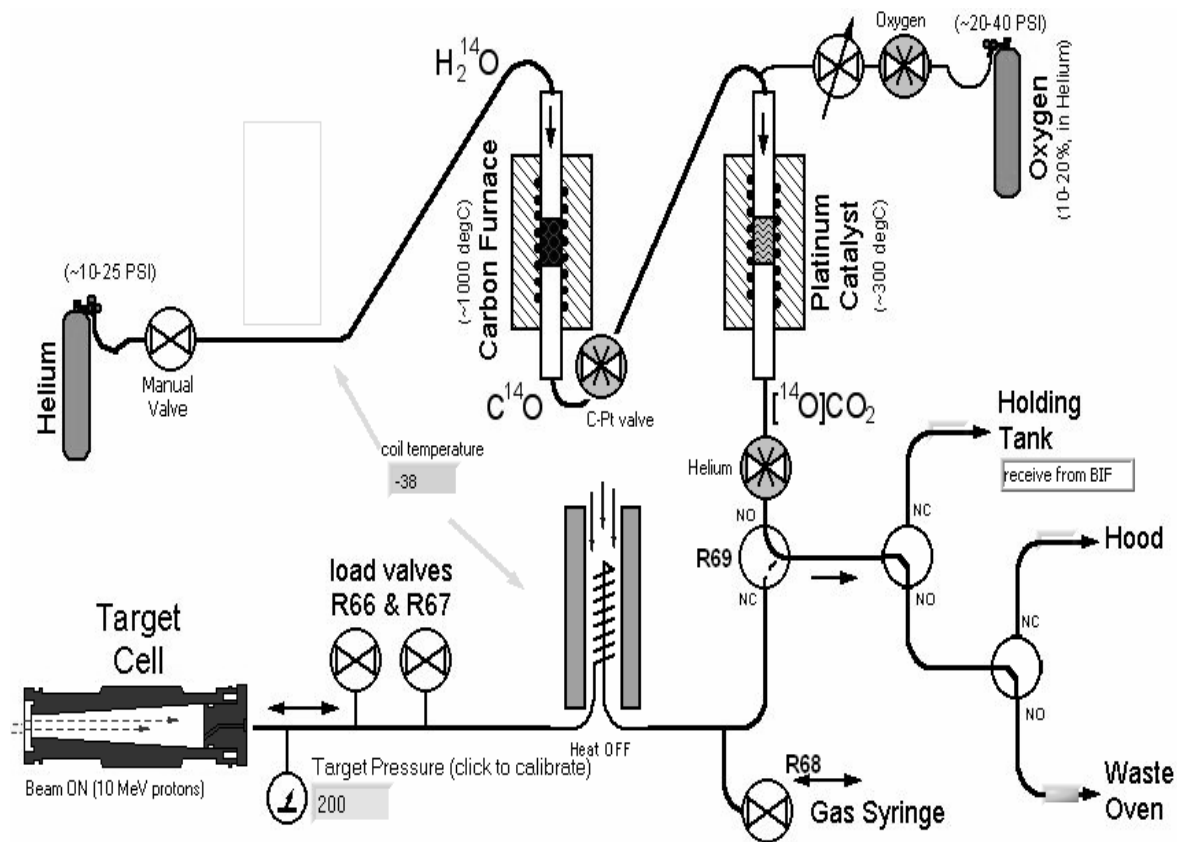
Figure 2.5 The system for production of $H_2^{14}O$ and conversion to $[^{14}O]CO_2$.
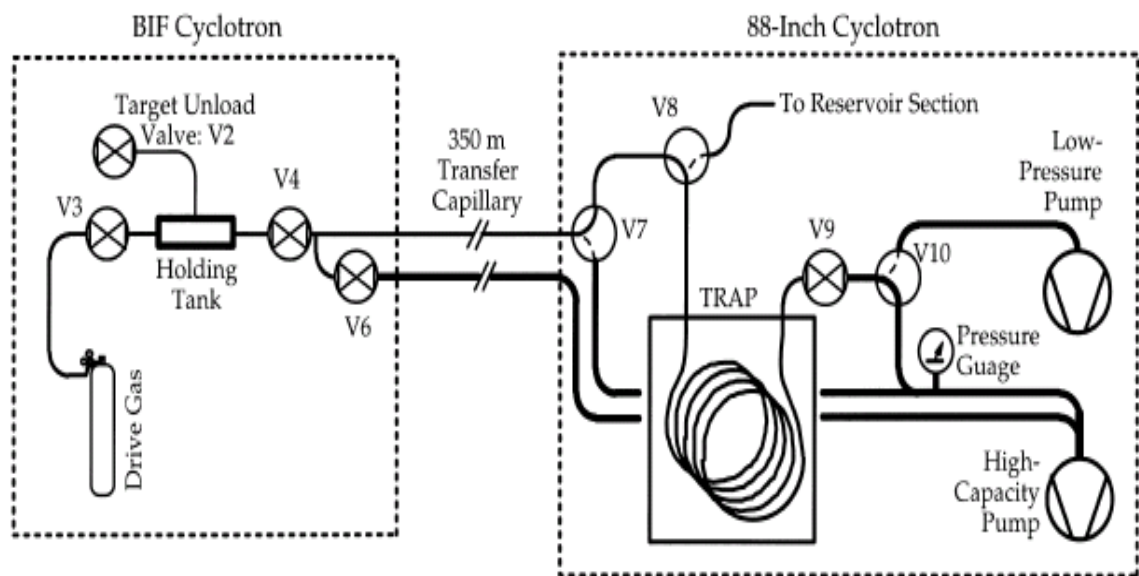
Figure 2.6 The system for transporting activity between the two accelerator buildings.

CHAPTER 3
Nuclear Reactions in Stars

3.1 Introduction

How were the elements from iron to uranium made? This is one of "The 11 Greatest Unanswered Questions of Physics," which were reported by the National Academy of Science in 2002 [Tu03]. Many scientists have been trying to explain the evolution of stars and the universe. The standard model of hot Big Bang theory gives us some clues to the origin of the universe, and nuclear physics has played a very important role in understanding the creation of elements via stellar nucleosynthesis.

Stars are the cooking pots of the universe, and nuclear reactions inside stars produce energy from synthesizing elements. In the 1920s, astrophysicists started to suspect that reactions among nuclear species were the source of the energy in stars [Ro88]. This suspicion led to considering an energy-producing mechanism that primarily involved hydrogen [At31]. Later, Bethe demonstrated in 1939 [Be39, see also Be38] that the energy source of the sun and similar stars is the fusion of hydrogen to helium. In 1957, Burbridge, Burbridge, Fowler and Hoyle published a famous paper, also known as B2FH [Bu57], in which they quantitatively explained many nuclear reaction sequences in stars.

This chapter will describe nuclear reactions which produce energy in stars. The hydrogen and helium burning processes are qualitatively presented, and basic concepts in nuclear astrophysics are introduced.

3.2 Hydrogen Burning

3.2.1 The p-p chain

In general, stars begin life as a mixture of hydrogen and 24% (by weight) helium (The Sun's composition is believed to be about 70% hydrogen and 28% helium by weight.). As this original gas cloud collapses, conversion of gravitational potential energy into kinetic energy increases the temperature of the cloud. As the temperature of star increases, protons are able to fuse with one another since their energy is now high enough to overcome the repulsive Coulomb barrier. The equilibrium between the outward pressure from the radiation released in fusion and the inward gravitational force allows stars to cease further collapse. Stars may last up to 10^{10} years in this phase [Kr88].

The p-p reaction (the proton-proton reaction) is the primary fusion reaction in the chain that changes four hydrogen nuclei into one helium nucleus (hydrogen burning). It is known that this reaction chain is the dominant process in the Sun (and similar size stars), generating 98.5% of the Sun's energy release. The p-p chain starts with the fusion of two protons to form a deuteron via the weak interaction, emitting a neutrino and a positron. The deuteron immediately fuses with another proton to form ^{3}He as follows.

$$p + p \rightarrow d + e^{+} + \nu$$
$$p + d \rightarrow {}^{3}He + \gamma$$

(3.1)

After this, two reaction branches are possible:

$$^{3}He + {}^{3}He \rightarrow {}^{4}He + 2p ,$$

(3.2)

or

$$^{3}He + {}^{4}He \rightarrow {}^{7}Be + \gamma .$$

(3.3)

The former is called the p-p I chain, and the latter is further split into two branches, which are the p-p II chain and the p-p III chain, respectively.

$$^3He + {}^4He \rightarrow {}^7Be + \gamma$$
$$^7Be + e^- \rightarrow {}^7Li + \nu \quad , \tag{3.4}$$
$$^7Li + p \rightarrow 2{}^4He$$

and

$$^3He + {}^4He \rightarrow {}^7Be + \gamma$$
$$^7Be + p \rightarrow {}^8B + \gamma$$
$$^8B \rightarrow {}^8Be + e^+ + \nu \tag{3.5}$$
$$^8Be \rightarrow 2{}^4He$$

However, the net results of the balanced reaction chains are the same for all three branches as follows.

$$4p \rightarrow {}^4He + 2e^+ + 2\nu + 2\gamma . \tag{3.6}$$

The dominance of a branch strongly depends on the stellar density and temperature. For example, it is known that the p-p I, p-p II and p-p III chains occur with frequencies of 86%, 14% and 0.02%, respectively, in the Sun [Ro88]. Figure 3.1 shows a diagram of the p-p chain.

3.2.2 The Hot p-p chain

For stellar temperatures higher than 0.03 T_9 (the Sun's temperature is about 0.015 T_9, where $T_9 = 10^9$ K), the p-p chain is dominated by the p-p III chain (discussed in section 3.2.1.) The ^{8}B nuclei quickly decay to ^{8}Be via β^+ decay ($T_{1/2} = 0.77$ sec.). For still higher

temperatures, it becomes quite probable for the ^{8}B nuclei to capture another proton and form ^{9}C. This is the starting point of the so called p-p IV chain. Its sequence is represented as follows.

$$^7Be(p,\gamma)^8B(p,\gamma)^9C(e^+\nu)^9B(p)^8Be(\alpha)^4He \, . \tag{3.7}$$

Another competing reaction is α-capture on ^{7}Be, forming ^{11}C. In this case also, the heaviest nuclide (^{11}C) produced in this sequence decays and returns to helium. This sequence is known as the p-p V chain, and expressed as [Wi89],

$$^7Be(\alpha,\gamma)^{11}C(e^+\nu)^{11}B(p,\alpha)^8B(\alpha)^4He \, . \tag{3.8}$$
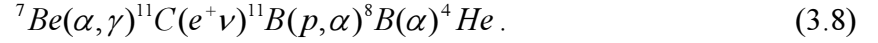
The reaction sequences which include the p-p III, p-p IV, and p-p V chains are known as the Hot p-p chain, and are the dominant hydrogen burning processes especially in supermassive non-metalicity (no elements heavier than helium) stars with mass of $10^5 \, \mathrm{M_\odot}$ ($\mathrm{M_\odot}$ = solar mass) or larger. In addition to these sequences, high stellar temperature (~ 0.1 T_9) allows competing reaction sequences to start such as

$$^7Be(\alpha,\gamma)^{11}C(p,\gamma)^{12}N(e^+\nu)^{12}C \, , \tag{3.9}$$

and, to a lesser extent

$$^7Be(p,\gamma)^8B(\alpha,p)^{11}C(p,\gamma)^{12}N(e^+\nu)^{12}C \, . \tag{3.10}$$
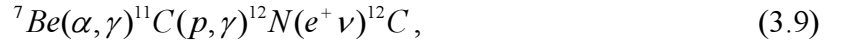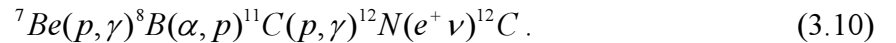
These "break-out" reactions from the Hot p-p chain to $A \geq 12$ regions were recognized as very important pathways to form ^{12}C in the absence of CNO nuclei, and the key reaction is proton capture on ^{11}C.

3.2.3 The CNO cycle

The CNO cycle was proposed by Bethe in 1939 [Be39]. It is another way to convert four hydrogen nuclei into one helium nucleus, but the CNO isotopes just act as catalysts in the reaction chain. Its net result is the same as the p-p chain, but it is now known that the CNO cycle becomes the dominant hydrogen burning process in somewhat more massive stars than our Sun. Figure 3.2 and Eq. (3.11) show the reaction sequence of the CNO cycle. The stellar temperature is lower than 0.08 T_9.

$$
\begin{aligned}
{}^{12}C + p &\rightarrow {}^{13}N + \gamma \\
{}^{13}N &\rightarrow {}^{13}C + e^+ + \nu \\
{}^{13}C + p &\rightarrow {}^{14}N + \gamma \\
{}^{14}N + p &\rightarrow {}^{15}O + \gamma \\
{}^{15}O &\rightarrow {}^{15}N + e^+ + \nu \\
{}^{15}N + p &\rightarrow {}^{12}C + {}^4He
\end{aligned}
\tag{3.11}
$$
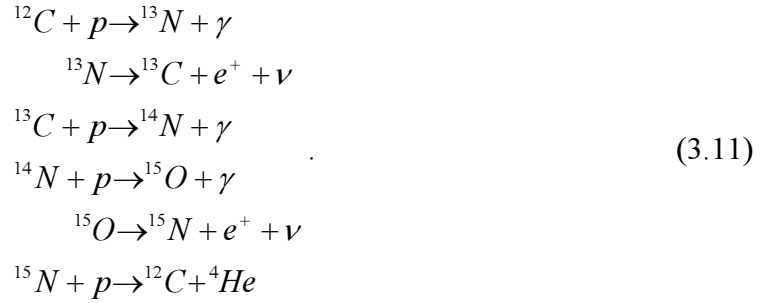
This sequence is limited by the β^+ decay of ^{13}N ($T_{1/2}$ = 10 min.) and ^{15}O ($T_{1/2}$ = 122 sec.). If the stellar temperature approaches 0.08-0.1 T_9, this cycle is limited by ^{14}O ($T_{1/2}$ = 71 sec.) and ^{15}O ($T_{1/2}$ = 122 sec.), leading to the Hot-CNO cycle.

$$
\begin{aligned}
{}^{12}C + p &\rightarrow {}^{13}N + \gamma \\
{}^{13}N + p &\rightarrow {}^{14}O + \gamma \\
{}^{14}O &\rightarrow {}^{14}N + e^+ + \nu \\
{}^{14}N + p &\rightarrow {}^{15}O + \gamma \\
{}^{15}O &\rightarrow {}^{15}N + e^+ + \nu \\
{}^{15}N + p &\rightarrow {}^{12}C + {}^4He
\end{aligned}
\tag{3.12}
$$
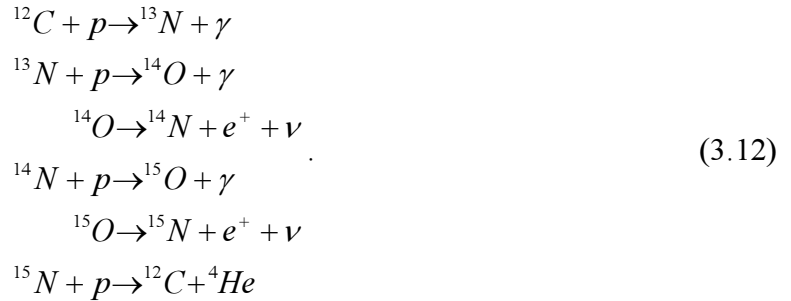
3.3 Helium Burning

Stars spend most of their lifetime burning hydrogen as source of energy, but as the hydrogen becomes depleted by the p-p chain and the CNO cycle, as described above, helium accumulates in the center of the stars. When the hydrogen burning state is completed, inward gravitational collapse starts in the core of the stars and the stellar temperature increases until the helium burning process is ignited (about 0.1-0.2 T_9). Hence, helium burning is mostly observed in old stars such as red giants.

The first step in the helium burning process is to fuse two helium nuclei into a ^{8}Be, but ^{8}Be is unstable and decays back to two helium nuclei with a time of the order of 10^{-16} seconds.

$$^4He + {}^4He \leftrightarrow {}^8Be \ . \tag{3.13}$$
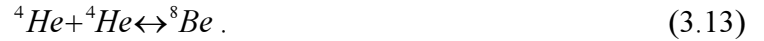
However, ^{8}Be may capture another helium before its decay.

$$^8Be + {}^4He \rightarrow {}^{12}C \ . \tag{3.14}$$

This is called the triple-alpha (3α) process, leading to the formation of ^{12}C. Heavier nuclei such as ^{16}O, or even ^{20}Ne, can be formed as by-products of additional helium capture by ^{12}C or ^{16}O, but these reactions are less likely since the Coulomb barrier increases with increasing nuclear charge.

3.4 The Astrophysical S-factor

The nuclear reaction cross section, σ, for the above very low energy nuclear reactions can be simply represented as a function that depends upon a geometrical factor, the properties of the nuclei involved in the reactions, and the Coulomb barrier penetrability. This has a basic form of

$$\sigma = \pi \lambdabar^2 \times \left| \langle nuclei \rangle \right|^2 \times P_\ell(E) \propto \frac{1}{E} \times \left| \langle nuclei \rangle \right|^2 \times \exp(-2\pi\eta), \tag{3.15}$$

where $\lambdabar = \dfrac{\hbar}{p} = \dfrac{\hbar}{\sqrt{2\mu E}}$, and $\eta = \sqrt{\dfrac{\mu}{2E}} \dfrac{Z_1 Z_2 e^2}{\hbar}$.

The geometrical factor is represented in terms of the reduced deBroglie wavelength, $\lambdabar$; and the penetrability for a given l value, P_ℓ, can be quantitatively evaluated using the Sommerfeld parameter, η. For example, the cross section for the direct capture reaction $A + x \rightarrow B + \gamma$ can be written as

$$\sigma(E) = \pi \lambdabar^2 \left| \langle B | H_\gamma | A + x \rangle \right|^2 P_\ell(E). \tag{3.16}$$

The matrix element contains the nuclear properties of the capture reaction. Therefore, an astrophysical S-factor, $S(E)$, is introduced in order to describe the physics of the nuclear interaction in the reaction cross section as follows.

$$\sigma(E) = \frac{1}{E} S(E) \exp(-2\pi\eta). \tag{3.17}$$

The penetrability strongly depends on the energy, and may decrease the cross section by orders of magnitude as the energy decreases. To obtain a quantity less dependent on the energy, the astrophysical S-factor is expressed in terms of the cross section by rearranging Eq. (3.17), obtaining

$$S(E) = E\sigma(E)\exp(2\pi\eta).$$ (3.18)

Consequently, $S(E)$ is less dependent on the energy than the cross section alone, so that it can be easily graphed, fitted and extrapolated over the relevant energy range.

3.5 The Stellar Reaction Rate

The astrophysical reaction rate $R(T)$ of $A(a,b)B$ at a temperature T can be written as

$$R(T) = \frac{N_A N_a}{1 + \delta_{Aa}} \langle \sigma v \rangle,$$ (3.19)

where N_i is the number density of the particle i, v is the relative velocity, and σ is the reaction cross section. The δ_{Aa} term arises for the special case of two identical species in the entrance channel. The quantity $\langle \sigma v \rangle$ is critical in calculating the stellar reaction rate, and is defined as

$$\langle \sigma v \rangle = \int \sigma(v)\phi(v)dv,$$ (3.20)

where $\phi(v)$ is the velocity distribution of the reacting particles. The reacting particles in a stellar environment are in thermal equilibrium at temperature T, and are described by a Maxwell-Boltzmann velocity distribution as follows.

$$\phi(v) = 4\pi \left(\frac{\mu}{2\pi k_B T} \right)^{3/2} v^2 \exp\left(-\frac{\mu v^2}{2k_B T} \right),$$ (3.21)

where μ is the reduced mass of the reacting particles and k_B is the Boltzmann constant.

By using $E = \frac{1}{2}\mu v^2$, $\langle \sigma v \rangle$ is given by [Ro88]

$$\langle \sigma v \rangle = \left(\frac{8}{\pi \mu} \right)^{1/2} \frac{1}{(k_B T)^{3/2}} \int_0^\infty \sigma(E) E \exp\left(-\frac{E}{k_B T} \right) dE$$

.   (3.22)

$$= \left(\frac{8}{\pi \mu} \right)^{1/2} \frac{1}{(k_B T)^{3/2}} \int_0^\infty S(E) \exp\left(-2\pi \eta - \frac{E}{k_B T} \right) dE$$

The integrand is a product of the cross section and the Maxwell-Boltzmann distribution. Since the cross section increases exponentially with energy while the Maxwell-Boltzmann distribution decreases exponentially with energy, this results in a function with peak at an energy of E_o, and width of ΔE_o. This quantity E_o is the effective energy for the nuclear reaction at a given temperature, and is known as the Gamow peak.

For a non-resonance reaction or a resonance reaction involving a broad state, the stellar reaction rate is calculated numerically after inserting a cross section into Eq. (3.22). However, for a resonance reaction involving a narrow state, the Maxwell-Boltzmann distribution and the resonance width are assumed to be constant over the resonance region. The Breit-Wigner formula [Br36] for a narrow resonance state is then used for the cross section, and its integration yields the following relatively simple result.

$$\langle \sigma v \rangle = \left(\frac{2\pi}{\mu kT} \right)^{3/2} \hbar^2 (\omega \gamma)_R \exp\left(-\frac{E_R}{k_B T} \right),$$ (3.23)

where $(\omega \gamma)_R$ is the resonance strength. It is composed of the spins and the resonance widths of the reacting particles and the compound nucleus for the reaction $A(a,b)B$, and is given by

$$(\omega \gamma)_R = \frac{2J+1}{(2j_A+1)(2j_a+1)} \frac{\Gamma_a \Gamma_b}{\Gamma_R}.$$ (3.24)

The total reaction rate is given by a sum of all contributions from non-resonance (NR) reactions, and resonance (R) reactions. In addition, interference terms between resonance reactions (mostly from broad resonant states) and non-resonance reactions are also considered if the same angular momentum is involved in both reactions. As a result, the total reaction rate is expressed as [Ro88]

$$\langle \sigma v \rangle_{tot} = \sum \langle \sigma v \rangle_{NR} + \sum \langle \sigma v \rangle_{R} + \langle \sigma v \rangle_{Interference}. \tag{3.25}$$

In order to explain the evolution of stars, accurate calculations of stellar reaction rates are necessary, and the astrophysical S-factor or the nuclear reaction cross section is the key factor as shown above. Many experimental studies involving very important nuclear reactions in the stellar evolution have provided the astrophysical S-factors and the stellar reaction rates as research outcomes (for example, $^7Be(p,\gamma)^8B$ [Xu94, Li96], $^{14}N(p,\gamma)^{15}O$ [Be02], and $^{11}C(p,\gamma)^{12}N$ [Le95, Li03, Ta03]). The astrophysical S-factor and the stellar reaction rate of the $^{11}C(p,\gamma)$ reaction based on our experiment at the BEARS facility are presented in Chapter 5 (see Figure 5.6 and Figure 5.7).
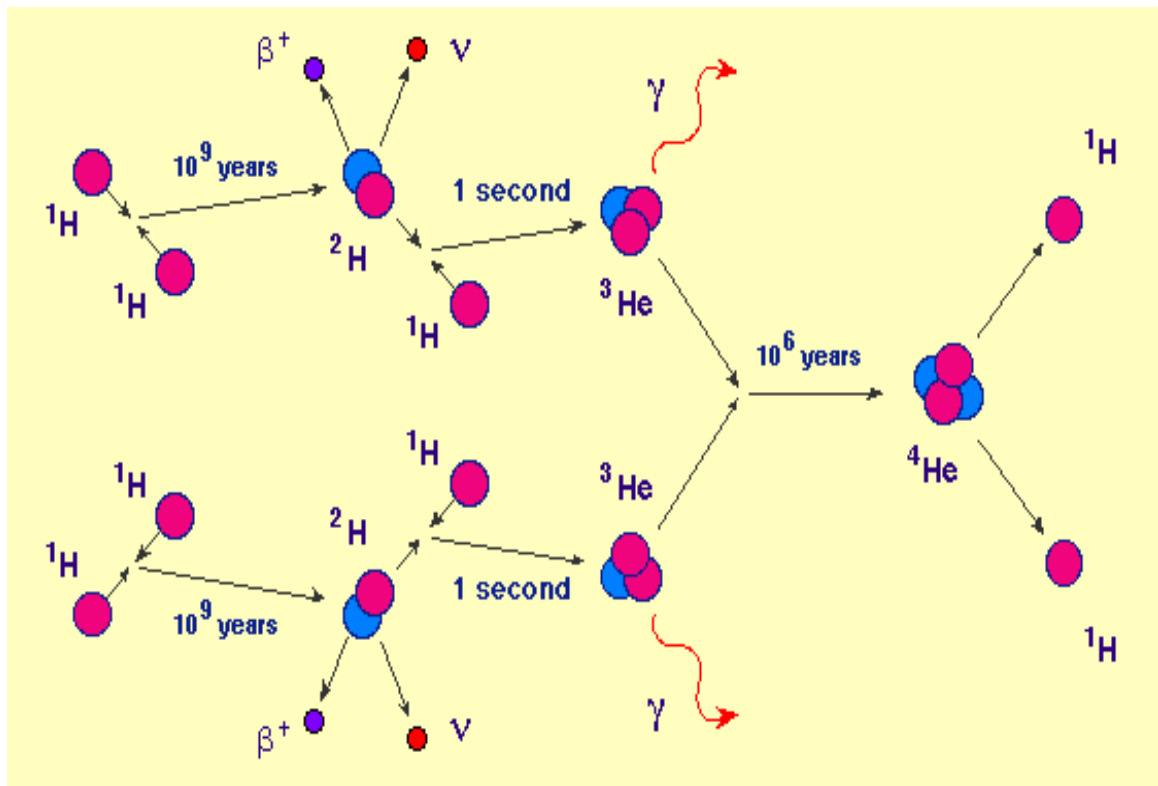
Figure 3.1 Diagram of the p-p chain reaction
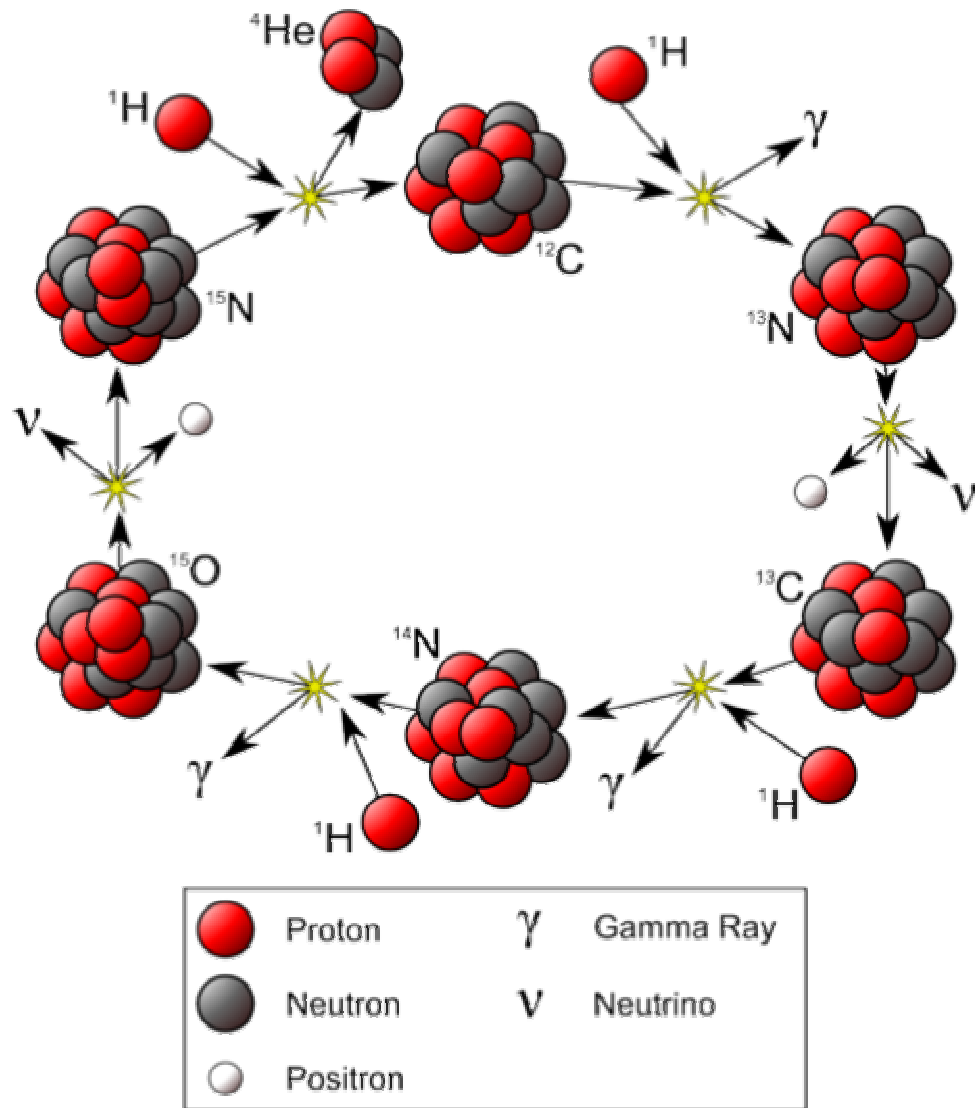
Figure 3.2 Diagram of the CNO cycle.

CHAPTER 4
Nuclear Reaction Theory

4.1 R-matrix Theory

4.1.1 Introduction

Lane and Thomas [La58] developed the modern theory of compound nucleus resonance reactions as an outgrowth of earlier work [Be36, Br36, Ka38, Wi47]. This approach has been called R-matrix theory [Wi47]. As presented by Land and Thomas, the nuclear reaction configuration space is divided into "internal" and "external" regions. The "internal" region corresponds to the compound nucleus per se, which includes the basic nuclear physics such as level energies, spins/parities, and level widths. The "external" region represents "channels" to or from the compound nucleus, which is related to penetration factors, Coulomb wave functions and so on. These two regions are matched at the surface of the nucleus using the boundary conditions.

4.1.2 External Region

The general solution for the interacting particles in the external region satisfies the following radial Schrödinger wave equation, including the Coulomb and centrifugal potentials.

$$\frac{du_\ell^2}{d^2 r} + \left[k^2 - \frac{2\eta k}{r} - \frac{\ell(\ell+1)}{r^2} \right] u_\ell = 0, \tag{4.1}$$

where $k = \dfrac{\sqrt{2mE}}{\hbar}$, and $\eta = \dfrac{Z_1 Z_2 e^2}{\hbar v}$. When $\rho = kr$ is substituted in Eq. (4.1), the solutions are the known regular and irregular Coulomb functions $F_\ell(\eta, \rho)$ and $G_\ell(\eta, \rho)$. Their asymptotic behavior at large r is:

$$
\begin{aligned}
F_l &\sim \sin[kr - \eta \ln(2kr) - (1/2)l\pi + \sigma_l] \\
G_l &\sim \cos[kr - \eta \ln(2kr) - (1/2)l\pi + \sigma_l]
\end{aligned}
\tag{4.2}
$$

where $\sigma_l = \arg[1 + l + i\eta] = \tan^{-1}\left(\dfrac{1+l}{\eta}\right)$.

In general, incoming (I_ℓ) and outgoing (O_ℓ) wavefunctions in the external region can be expressed in terms of Coulomb functions based on their asymptotic behavior at large r:

$$
\begin{aligned}
I_\ell &= (G_\ell - iF_\ell)\exp(i\omega_\ell) \\
O_\ell &= (G_\ell + iF_\ell)\exp(-i\omega_\ell)
\end{aligned}
\tag{4.3}
$$

with $\omega_\ell = \displaystyle\sum_{n=1}^{\ell} \arctan\left(\dfrac{\eta}{n}\right)$, $\ell > 0$.

Finally, a general solution Ψ_ℓ may always be expressed as a linear combination of incoming and outgoing wavefunctions, and given by

$$
\Psi_\ell = I_\ell - U_\ell O_\ell,
\tag{4.4}
$$

where U_ℓ is called the collision function (or collision matrix in a general multi-channel case) and is discussed in section 4.1.4. The boundary condition (logarithmic derivative) at the radius a is then given by

$$
\left(\frac{\rho \Psi'(\rho)}{\Psi(\rho)}\right)_{\rho=ka} = \frac{\rho I_l' - \rho U_l O_l'}{I_l - U_l O_l}\bigg|_{\rho=ka}.
\tag{4.5}
$$

4.1.3 Internal Region

4.1.3.1 Elastic Scattering of Spinless Particles

As an initial approach to the R-matrix framework, a simple case can be utilized as an example before discussing general R-matrix theory. General R-matrix theory accounts for all possible reactions, and includes reacting particles whose spins are non-zero. Therefore, elastic scattering (single channel) between spinless particles by general central potentials is the easiest case, but includes all the underlying principles.

The radial parts $r^{-1}u(r)$ of two internal wave functions with a central potential V (r) at the two energies E_1 and E_2 will satisfy the Schrödinger equation as follows:

$$\left(\frac{d^2u_1}{dr^2}\right)+\frac{2M}{\hbar^2}(E_1-V(r))u_1=0$$
$$\left(\frac{d^2u_2}{dr^2}\right)+\frac{2M}{\hbar^2}(E_2-V(r))u_2=0$$

$$(4.6)$$

where M is the reduced mass. If the first of these is multiplied by u_2 and the second by u_1, and the difference is then integrated from 0 to the channel radius a :

$$\int_0^a\left(u_2\frac{d^2u_1}{dr^2}-u_1\frac{d^2u_2}{dr^2}\right)dr+\frac{2M}{\hbar^2}(E_1-E_2)\int_0^a u_1u_2dr=0 .$$

$$(4.7)$$

Partial integration of the first integral results in

$$\left(u_2\frac{du_1}{dr}-u_1\frac{du_2}{dr}\right)\bigg|_{r=a}+\frac{2M}{\hbar^2}(E_1-E_2)\int_0^a u_1u_2dr=0 .$$

$$(4.8)$$

If u_λ and $u_{\lambda'}$ are two different eigenfunctions, which correspond to two different eigenvalues E_λ and $E_{\lambda'}$, respectively, u_λ and $u_{\lambda'}$ are orthonormal in the internal region:

$$\int_0^a u_\lambda u_{\lambda'}dr=\delta_{\lambda\lambda'}$$

$$(4.9)$$

Their boundary condition is set to be

$$a\left(\frac{du_\lambda(r)}{dr}\right)\bigg|_{r=a} = Bu_\lambda(a),$$ (4.10)

where B is a real number.

The solution of the Schrödinger equation at any given energy E, $u_E(r)$, can be expressed using a complete set of eigenfunctions in the internal region, and represented by

$$u_E(r) = \sum_\lambda A_\lambda u_\lambda(r), \quad 0 \le r \le a$$ (4.11)

where $A_\lambda = \int_0^a u_\lambda u_E dr$.

By applying Eq. (4.8) to u_λ and u_E,

$$\left(u_E\frac{du_\lambda}{dr} - u_\lambda\frac{du_E}{dr}\right)\bigg|_{r=a} + \frac{2M}{\hbar^2}(E_\lambda - E)\int_0^a u_\lambda u_E dr = 0,$$ (4.12)

and

$$A_\lambda = \int_0^a u_\lambda u_E dr = \frac{\hbar^2}{2M}\frac{u_\lambda}{(E_\lambda - E)}\left(\frac{du_E}{dr} - \frac{u_E}{u_\lambda}\frac{du_\lambda}{dr}\right)_{r=a}$$
$$= \frac{\hbar^2}{2M}\frac{u_\lambda}{(E_\lambda - E)}\left(\frac{du_E}{dr} - \frac{B}{a}u_E\right)_{r=a}$$ (4.13)

using the boundary condition Eq. (4.10).

Inserting Eq. (4.13) into (4.11) results in

$$u_E(r) = G(r,a)\left(a\frac{du_E}{dr} - Bu_E\right)_{r=a},$$ (4.14)

where $G(r,a) = \dfrac{\hbar^2}{2Ma} \sum_\lambda \dfrac{u_\lambda(r)u_\lambda(a)}{(E_\lambda - E)}$ is the Green's function which relates the value of

the wave function in the internal region to its derivative on the surface. Finally, the R-function is defined as

$$R \equiv G(a,a) = \sum_\lambda \frac{\gamma_\lambda{}^2}{(E_\lambda - E)}, \tag{4.15}$$

where $\gamma_\lambda = \left(\dfrac{\hbar^2}{2Ma}\right)^{1/2} u_\lambda(a)$ is the reduced width amplitude.

4.1.3.2 General Case of Elastic Scattering

The case of elastic scattering of spinless particles can be easily generalized to take account of the spins and reaction channels. As stated in Eq. (4.6) in the previous section, the wave equation for a system at two energies is expressed by

$$\begin{aligned} H\Psi_1 &= E_1\Psi_1 \\ H\Psi_2 &= E_2\Psi_2 \end{aligned}, \tag{4.16}$$

where H is the Hamiltonian operator. The first of these is multiplied by Ψ_2^* and the complex-conjugate of the second by Ψ_1. The difference between the resulting equations is integrated over the internal region τ :

$$(E_2 - E_1)\int_\tau \Psi_2^*\Psi_1 d\tau = \int_\tau [(H\Psi_2)^*\Psi_1 - \Psi_2^* H\Psi_1]d\tau, \tag{4.17}$$

and Eq. (4.17) is then represented in terms of a surface integral at the channel surface S :

$$(E_2 - E_1)\int_\tau \Psi_2^*\Psi_1 d\tau = \int_S \frac{\hbar^2}{2M}(\Psi_2^*\nabla\Psi_1 - \Psi_1\nabla\Psi_2^*)dS = \sum_c (V_{2c}^* D_{1c} - V_{1c} D_{2c}^*), \tag{4.18}$$

where $V_c = \left(\dfrac{\hbar^2}{2M_c a_c}\right)^{1/2} \int \varphi_c^* \Psi dS$, and $D_c = \left(\dfrac{\hbar^2}{2M_c a_c}\right)^{1/2} \int \varphi_c^* \nabla(r_c \Psi) dS$ (V_c and D_c are

found to be real). The last equality follows by substitution of the surface representations

for Ψ and $\nabla \Psi$ in terms of the assumed complete set of surface functions φ_c:

$$\Psi = \sum_c \left(\frac{2M_c a_c}{\hbar^2}\right)^{1/2} V_c \varphi_c$$
$$\nabla \Psi = \sum_c \left(\frac{2M_c}{a_c \hbar^2}\right)^{1/2} (D_c - V_c)\varphi_c$$
$$(4.19)$$

In this case, the general boundary condition is given by

$$\frac{D_{\lambda c}}{V_{\lambda c}} = B_c \tag{4.20}$$

By applying these fundamental equations to any two proper solutions X_λ, and $X_{\lambda'}$

belonging to energy values E_λ, and $E_{\lambda'}$, a wave function Ψ can be expressed as a

complete set as in Eq. (4.11). That is,

$$\Psi = \sum_\lambda A_\lambda X_\lambda , \tag{4.21}$$

where $A_\lambda = \int_\tau X_\lambda^* \Psi d\tau$, and $\int_\tau X_{\lambda'}^* X_\lambda d\tau = \delta_{\lambda\lambda'}$ again.

This coefficient A_λ is determined by applying Eq. (4.18) to the solution Ψ of energy E

and the solution X_λ of energy E_λ as is shown in Eq. (4.12) and Eq. (4.13).

$$(E_\lambda - E)\int_\tau X_\lambda^* \Psi d\tau = (E_\lambda - E)\int_\tau X_\lambda^* \sum_\lambda A_\lambda X_\lambda d\tau = \sum_c (V_{\lambda c}^* D_c - V_c D_{\lambda c}^*). \tag{4.22}$$

Then, we find the coefficient A_λ as follows.

$$A_\lambda = \frac{1}{(E_\lambda - E)} \sum_c (V_{\lambda c}^* D_c - V_c D_{\lambda c}^*)$$

$$= \frac{1}{(E_\lambda - E)} \sum_c V_{\lambda c}^* (D_c - V_c \frac{D_{\lambda c}^*}{V_{\lambda c}^*}) \quad , \tag{4.23}$$

$$= \frac{1}{(E_\lambda - E)} \sum_c \gamma_{\lambda c} (D_c - B_c V_c)$$

where $\dfrac{D_{\lambda c}^*}{V_{\lambda c}^*} = \dfrac{D_{\lambda c}}{V_{\lambda c}} = B_c$ and $\gamma_{\lambda c} = V_{\lambda c}^* = V_{\lambda c} = \left(\dfrac{\hbar^2}{2 M_c a_c}\right)^{1/2} \int \varphi_c^* X_\lambda dS$.

Therefore, Eq. (4.22) is expressed by

$$\Psi = \frac{1}{(E_\lambda - E)} \sum_\lambda \sum_c \gamma_{\lambda c} (D_c - B_c V_c) X_\lambda$$

$$= \sum_c \left[\left(\sum_\lambda \frac{\gamma_{\lambda c} X_\lambda}{(E_\lambda - E)} \right) (D_c - B_c V_c) \right] \quad , \tag{4.24}$$

By operating on Eq. (4.24) with $\int_S \varphi_{c'}^* dS$,

$$\left(\frac{\hbar^2}{2 M_{c'} a_{c'}}\right)^{1/2} \int_S \varphi_{c'}^* \Psi dS$$

$$= \sum_c \left[\left(\sum_\lambda \frac{\gamma_{\lambda c}}{(E_\lambda - E)} \times \left(\frac{\hbar^2}{2 M_{c'} a_{c'}}\right)^{1/2} \int_S \varphi_{c'}^* X_\lambda dS \right) (D_c - B_c V_c) \right]. \tag{4.25}$$

$$= \sum_c \left[\left(\sum_\lambda \frac{\gamma_{\lambda c} \gamma_{\lambda c'}}{(E_\lambda - E)} \right) (D_c - B_c V_c) \right]$$

where $\gamma_{\lambda c'} = \left(\dfrac{\hbar^2}{2 M_{c'} a_{c'}}\right)^{1/2} \int \varphi_{c'}^* X_\lambda dS$.

Finally, the R-function for the general case with reaction channel spins c and c' is then defined by

$$R_{c'c} \equiv \sum_\lambda \frac{\gamma_{\lambda c'} \gamma_{\lambda c}}{(E_\lambda - E)}. \tag{4.26}$$

This generalized R-function reproduces Eq. (4.15) when c' is equal to c (elastic scattering of spinless particles).

4.1.4 The Collision Matrix

At the matching radius of the internal and external regions, the logarithmic derivative of the internal wavefunction is obtained by Eq. (4.14):

$$u(a) = G(a,a)\left(a\frac{du}{dr} - Bu \right)_{r=a} = R\left(a\frac{du}{dr} - Bu \right)_{r=a}, \qquad (4.25)$$

and therefore,

$$\frac{\left(a\frac{du}{dr} \right)_{r=a}}{u(a)} = \frac{1+BR}{R}. \qquad (4.26)$$

This must be matched to that of the external wavefunction using Eq. (4.5), and these two equations are replaced by

$$\left(\frac{\rho \Psi'(\rho)}{\Psi(\rho)} \right)_{\rho=ka} = \frac{\rho I_l' - \rho U_l O_l'}{I_l - U_l O_l} = \frac{1+BR}{R}, \qquad (4.27)$$

where $\rho = kr$.

As a result, a collision function U_l can be expressed in terms of the R-function:

$$U_l = \frac{I_l + I_l BR - \rho I_l' R}{O_l + O_l BR - \rho O_l' R} = \frac{I_l}{O_l} \frac{1 - \left(\frac{\rho I_l'}{I_l} - B \right) R}{1 - \left(\frac{\rho O_l'}{O_l} - B \right) R} = \frac{I_l}{O_l} \frac{1 - L_l^* R}{1 - L_l R}, \qquad (4.28)$$

where $L_l \equiv \left. \frac{\rho O_l'}{O_l} \right|_{ka} - B$ and $L_l^* \equiv \left. \frac{\rho I_l'}{I_l} \right|_{ka} - B$

For the general case with an incoming channel c and an outgoing channel c', the complete collision matrix is expressed as follows [Vo62]

$$U_{cc'} = \rho^{1/2} \frac{I_{c'}}{O_c} \rho^{-1/2} \frac{1 - L * R}{1 - LR} = e^{i(\Omega_c + \Omega_{c'})} P_c^{1/2} \frac{1 - L * R}{1 - LR} P_{c'}^{-1/2}, \qquad (4.29)$$

where $\Omega_c \equiv \omega_c - \phi_c$ is the scattering phase shift with $\phi_c = \arctan\left(\dfrac{F_c}{G_c}\right)$ and

$\omega_c = \sum\limits_{n=1}^{\ell} \arctan\left(\dfrac{\eta}{n}\right)$, $\ell > 0$. In Eq. (4.29), all the expressions are diagonal matrices except

for the R-matrix, and **1** is the diagonal unit matrix. $P_c \equiv \dfrac{\rho_c}{F_c^2 + G_c^2}$ is the (Coulomb)

penetration factor, $S_c \equiv \dfrac{P_c}{F_c F_c' + G_c G_c'}$ is the shift function and L_c is now defined as

$L_c \equiv S_c - B_c + iP_c$.

4.1.5 Differential Cross Section of the Nuclear Reaction

The general differential cross section of a nuclear reaction can be given by

$$\frac{d\sigma_{\alpha s \alpha' s'}}{d\Omega_{\alpha'}} = \frac{\pi}{(2s+1)k_\alpha^2} \times |CT + RT + IT|, \qquad (4.30)$$

for a wavenumber k_α, and an incoming (outgoing) particle channel α (α') with channel spin s (s') [La58].

CT is a Coulomb term, and obtained by

$$CT = (2s+1)|C_{\alpha'}(\theta_{\alpha'})|^2 \delta_{\alpha s \alpha' s'}, \qquad (4.31)$$

where $\theta_{\alpha'}$ is the center-of-mass angle of the outgoing channel. The Coulomb factor $C_{\alpha'}(\theta_{\alpha'})$ is expressed by

$$C_\alpha(\theta_\alpha) = \frac{1}{\sqrt{4\pi}}\eta_\alpha \sin -2\left(\frac{\theta_\alpha}{2}\right)\exp\left[-2i\eta_\alpha \ln(\sin\frac{\theta}{2})\right], \qquad (4.32)$$

where $\eta_\alpha = \dfrac{Z_1 Z_2 e^2}{\hbar v}$.

Eq. (4.32) becomes exactly the same as the Rutherford scattering cross section if the resonance term RT and the interference term IT are ignored.

The resonant term RT is given by

$$RT = \frac{1}{\pi}\sum_L B_L(\alpha s, \alpha' s')P_L(\cos(\theta_{\alpha'})), \qquad (4.33)$$

with the Legendre polynomials $P_L(\cos(\theta_{\alpha'}))$ and the resonance coefficient $B_L(\alpha s, \alpha' s')$ which is

$$B_L(\alpha s, \alpha' s') = \frac{1}{4}(-1)^{s-s'}\sum_{J_1 J_2 l_1 l_2 l_1' l_2'}\overline{Z}(l_1 J_1 l_2 J_2, sL)\overline{Z}(l_1' J_1 l_2' J_2, s'L)\times(T^{J_1}_{\alpha s l_1, a's'l_1'})(T^{J_2}_{\alpha s l_2, a's'l_2'})^*. \quad (4.34)$$

The transition matrix element $T^J_{\alpha s l, a's'l'}$ is related to the collision matrix element as follows.

$$T^J_{\alpha s l, a's'l'} = e^{2i\omega_{al}}\delta_{\alpha s l, \alpha's'l'} - U^J_{\alpha s l, \alpha's'l'}. \qquad (4.35)$$

The angular distribution coefficient $\overline{Z}(l_1 J_1 l_2 J_2, sL)$ is expressed by

$$\overline{Z}(l_1 J_1 l_2 J_2, sL) = (-1)^{l_1+l_2+J_1+J_2}\times(2L+1)^{1/2}(2l_1+1)^{1/2}(2l_2+1)^{1/2}(2J_1+1)^{1/2}(2J_2+1)^{1/2}$$
$$\times\begin{pmatrix}l_1 & l_2 & L \\ 0 & 0 & 0\end{pmatrix}\begin{Bmatrix}l_1 & l_2 & L \\ J_2 & J_1 & s\end{Bmatrix},$$

$$(4.36)$$

with the 3j symbols ( ) and the 6j symbols { }.

The interference term IT is given by [Ru05]

42

$$IT = -\delta_{\alpha s l, \alpha' s' l'} \frac{1}{\sqrt{4\pi}} \sum_{Jl} (2J+1) \times 2\,\mathrm{Re}\Big[i(T^J_{\alpha s l, \alpha' s' l'})^* C_{\alpha'}(\theta_{\alpha'}) P_l(\cos\theta_{\alpha'})\Big]. \qquad (4.37)$$

Eq. (4.30) is then summed over the s' and averaged with respect to the s to obtain the differential cross section for the nuclear reaction $\alpha \to \alpha'$ [Bl52], leading to

$$\frac{d\sigma_{\alpha\alpha'}}{d\Omega_{\alpha'}} = \frac{1}{(2I_1+1)(2I_2+1)} \times \sum_{ss'} \frac{d\sigma_{\alpha s \alpha' s'}}{d\Omega_{\alpha'}}, \qquad (4.38)$$

where I_1 and I_2 are the spins of the particles in the reaction channel α.

The theoretical differential cross sections from Eq. (4.38) are then compared to experimental data. For examples, data from a few elastic resonance scattering experiments [Te03, Gu05], are shown in Figure 4.1 to Figure 4.3 along with the theoretical R-matrix cross sections.
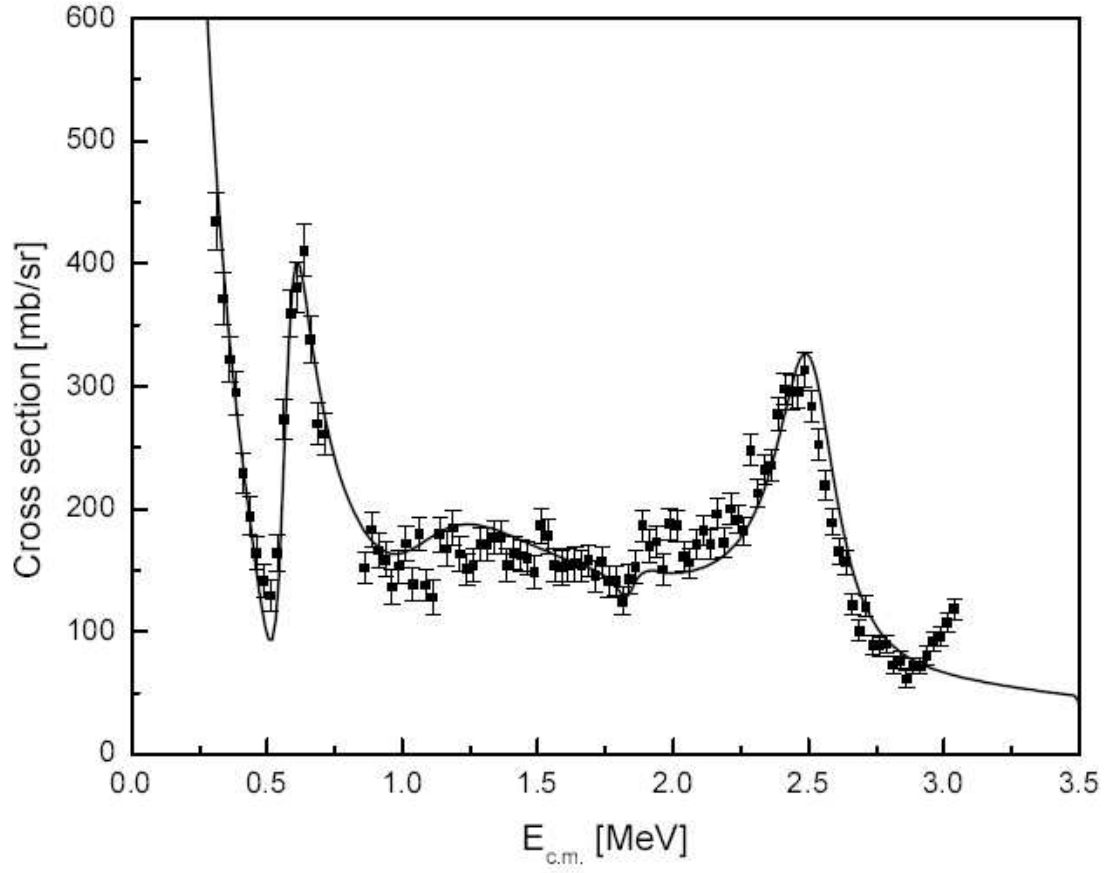
Figure 4.1 ^{11}C+p$\rightarrow$^{12}N elastic resonance scattering. The black squares with error bars are experimental data from Ref. [Te03] for $J^{\pi} = 3/2^{-}$ ^{11}C plus $J^{\pi} = 1/2^{+}$ proton elastic scattering. The solid line is obtained from our R-matrix calculation. Good agreement is clearly shown for four states in ^{12}N up to 2.8 MeV (see reference for more details).
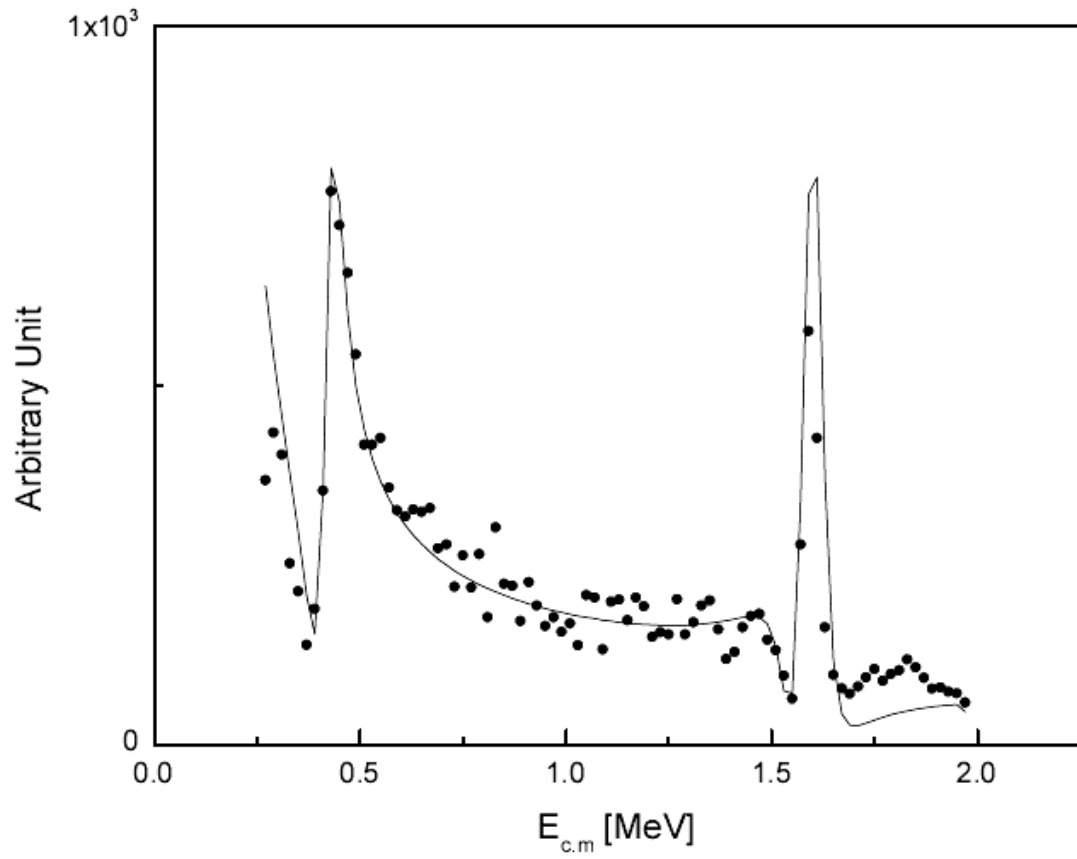
Figure 4.2 ^{12}C+p elastic resonance scattering. The black circles show our experimental data in arbitrary units. The solid line is from the R-matrix analysis. Note that an interference between the Coulomb and the resonance scattering is clearly observed around 0.4 MeV and 1.5 MeV.
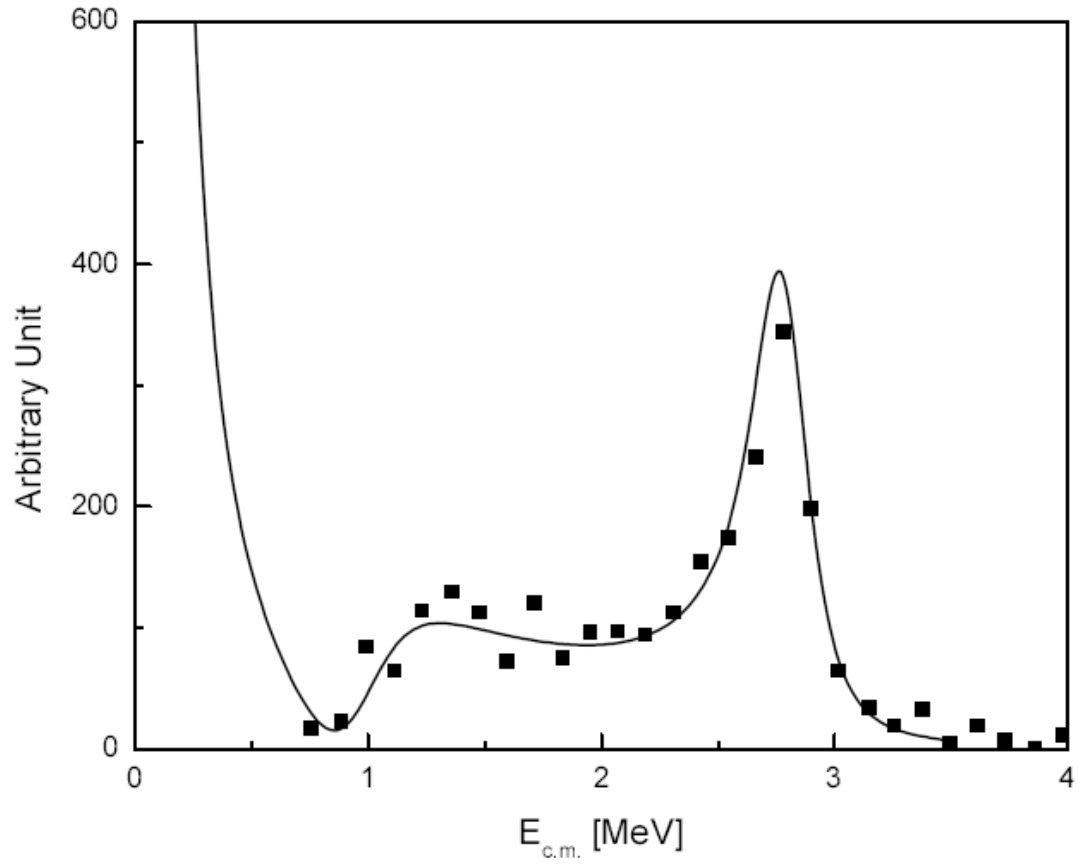
Figure 4.3 ^{14}O+p$\rightarrow$^{15}F elastic resonance scattering. The black squares represent experimental data. The broad peak around 1.23 MeV is a 1/2$^+$ state, and the large peak around 2.8 MeV is a 5/2$^+$ state in ^{15}F (see text). The solid line is from the R-matrix analysis.

4.2 Asymptotic Normalization Coefficient Method

4.2.1 Introduction

Peripheral nucleon transfer reactions have been used for more than a decade to extract spectroscopic information. Most transfer reactions have been analyzed within the framework of the Distorted-wave Born Approximation (DWBA), and experimental spectroscopic factors were compared with theoretical predictions in order to establish the spins and parities of nuclear states. The DWBA analysis gives the J^{π} values very well for states with a major (single particle) configuration, but does not give the true spectroscopic factor nearly as well. It has also been known that these extracted spectroscopic factors were strongly dependent on the optical model potential parameters used in the DWBA analysis, such as the Woods-Saxon potential parameters. In addition, the spectroscopic factor is strongly dependent on the behavior of the overlap function of the bound state wavefunctions within the nucleus. Hence, it is difficult to get an accurate spectroscopic factor with a DWBA analysis because a peripheral transfer reaction predominantly occurs at the surface of a nucleus. The Asymptotic Normalization Coefficient (ANC) is another important nuclear property that can be obtained from a peripheral transfer reaction, and it is independent of the potential model unlike the spectroscopic factor.

ANC's have been studied in few-nucleon systems such as the deuteron, triton, ^{3}He and so on, but, recently, the ANC method coupled with transfer reactions became a very useful tool to study direct radiative capture cross sections. The astrophysical radiative capture reaction is strongly dependent on the behavior of the tail of the nuclear overlap

47

function, which is given by the ANC. As a result, radiative capture cross sections can be determined by measuring the ANC. In addition, the ANC can be obtained from transfer reactions whose cross sections are orders of magnitude larger than direct radiative capture reactions.

4.2.2 Theoretical Approach

The theoretical scheme for using peripheral transfer reactions to extract ANCs can be represented within the framework of a DWBA analysis. For the transfer reaction $X + A \rightarrow Y + B$, where $X = Y + a$, $B = A + a$, where a is the transferred particle, the DWBA amplitude is given by [Mu97]

$$M(E_i, \cos\theta) = \sum_{M_a} \left\langle \chi_f^{(-)} I_{Aa}^B \left| \Delta V \right| I_{Ya}^X \chi_i^{(+)} \right\rangle. \tag{4.39}$$

E_i is the relative kinetic energy of particles X and A, θ is the scattering angle in the center of mass, $\chi_i^{(+)}$ and $\chi_f^{(-)}$ are the distorted waves in the initial and final channels, and ΔV is the transition operator.

Following the presentation in Ref. [Mu97], the overlap function I of the bound state wave functions of particle α ($\alpha = \beta + \gamma$), is represented as follows.

$$
\begin{aligned}
I_{\beta\gamma}^{\alpha}(\mathbf{r}_{\beta\gamma}) &= \left\langle \varphi_\beta(\zeta_\beta)\varphi_\gamma(\zeta_\gamma) \left| \varphi_\alpha(\zeta_\beta, \zeta_\gamma; \mathbf{r}_{\beta\gamma}) \right. \right\rangle \\
&= \sum_{l_\alpha m_{l_\alpha} j_\alpha m_{j_\alpha}} \left\langle J_\beta M_\beta j_\alpha m_{j_\alpha} \left| J_\alpha M_\alpha \right. \right\rangle \times \left\langle J_\gamma M_\gamma l_\alpha m_{l_\alpha} \left| j_\alpha m_{j_\alpha} \right. \right\rangle \ i^{l_\alpha} Y_{l_\alpha m_{l_\alpha}}(\hat{\mathbf{r}}_{\beta\gamma}) I_{\beta l_\alpha j_\alpha}^{\alpha}(r_{\beta\gamma})
\end{aligned} \tag{4.40}
$$

where φ is the bound state wave function; ζ is a set of internal coordinates including spin-isospin variables; and J and M are the spin and spin projection. Also $\hat{\mathbf{r}} = \mathbf{r}/r$, $\mathbf{r}_{\beta\gamma}$ is the relative coordinate of the center of mass of nuclei β and γ, j_α and m_{j_α} are

the total angular momentum of particle γ and its projection in the nucleus α. l_α and m_{l_α} are the orbital angular momentum of the relative motion of particles β and γ and its projection in the nucleus α. $\langle j_1 m_1 j_2 m_2 | j_3 m_3 \rangle$ is a Clebsch-Gordan coefficient, $Y_{l_\alpha m_{l\alpha}}(\hat{\mathbf{r}}_{\beta\gamma})$ is a spherical harmonic, and $I^\alpha_{\beta l_\alpha j_\alpha}(r_{\beta\gamma})$ is the radial overlap function.

The radial overlap wave function is usually approximated by the spectroscopic factor and a bound state wave function of the relative motion of β and γ as

$$I^\alpha_{\beta l_\alpha j_\alpha}(r_{\beta\gamma}) = S^{1/2}_{\beta l_\alpha j_\alpha}\varphi_{n_\alpha l_\alpha j_\alpha}(r_{\beta\gamma}). \tag{4.41}$$

The ANC method is model independent approach, and the radial overlap function $I^\alpha_{\beta l_\alpha j_\alpha}(r_{\beta\gamma})$ is given in terms of the asymptotic normalization coefficient $C^\alpha_{\beta l_\alpha j_\alpha}$ as follows.

$$I^\alpha_{\beta l_\alpha j_\alpha}(r_{\beta\gamma}) \overset{r_{\beta\gamma}>R_N}{\rightarrow} C^\alpha_{\beta l_\alpha j_\alpha} \frac{W_{-\eta_\alpha, l_\alpha+1/2}(2\kappa_\beta r_{\beta\gamma})}{r_{\beta\gamma}}, \tag{4.42}$$

where R_N is the nuclear interaction radius between β and γ, $W_{-\eta_\alpha, l_\alpha+1/2}(2\kappa_\beta r_{\beta\gamma})$ is the Whittaker function describing the asymptotic behavior of the bound state wave function of two charged particles, $\kappa_{\beta\gamma} = \sqrt{2\mu_{\beta\gamma}\varepsilon_{\beta\gamma}}$ is the wave number of the bound state $\alpha = (\beta\gamma)$, $\mu_{\beta\lambda}$ is the reduced mass of particles β and γ, and $\eta_{\beta\gamma} = Z_\beta Z_\gamma \mu_{\beta\gamma}/\kappa_{\beta\gamma}$ is the Coulomb parameter of the bound state $\alpha = (\beta\gamma)$. The ANC $C^\alpha_{\beta l_\alpha j_\alpha}$ is also related to the nuclear vertex constant (VNC) $G^\alpha_{\beta l_\alpha j_\alpha}$ by

$$G^\alpha_{\beta l_\alpha j_\alpha} = -e^{i\pi[(l_\alpha+\eta_\alpha)/2]} \frac{\sqrt{\pi}}{\mu_\alpha} C^\alpha_{\beta l_\alpha j_\alpha}. \tag{4.43}$$

The bound state wave function is also approximated by a Whittaker function as

$$\varphi_{n_\alpha l_\alpha j_\alpha}(r_{\beta\gamma}) \overset{r_{\beta\gamma}>R_N}{\rightarrow} b_{\beta l_\alpha j_\alpha} \frac{W_{-\eta_\alpha, l_\alpha+1/2}(2\kappa_\beta r_{\beta\gamma})}{r_{\beta\gamma}}, \tag{4.44}$$

where $b_{\beta \mathit{l}_\alpha j_\alpha}$ is the single-particle ANC. Figure 4.4 shows the bound state wave function approximated by the Whittaker function and the single-particle ANC. Therefore, the relationship between the ANC and the spectroscopic factor is given by

$$C^\alpha_{\beta \mathit{l}_\alpha j_\alpha} = (S_{\beta \mathit{l}_\alpha j_\alpha})^{1/2} b_{\beta \mathit{l}_\alpha j_\alpha}. \tag{4.45}$$

In the conventional DWBA analysis, the cross section is expressed as

$$\left(\frac{d\sigma}{d\Omega}\right)_{\exp} = \sum_{j_B j_X} S_{Aal_B j_B} S_{Yal_X j_X} \left(\frac{d\sigma}{d\Omega}\right)_{DWBA}. \tag{4.46}$$

The DWBA cross section strongly depends on the bound state potential chosen in the analysis and on the behavior of single-particle ANC. Eq. (4.46) is then parameterized in terms of the ANC, and is represented as follows.

$$
\begin{aligned}
\left(\frac{d\sigma}{d\Omega}\right)_{\exp} &= \sum_{j_B j_X} \left(\frac{C^B_{Aal_B j_B}}{b_{Aal_B j_B}}\right)^2 \left(\frac{C^X_{Yal_X j_X}}{b_{Yal_X j_X}}\right)^2 \left(\frac{d\sigma}{d\Omega}\right)_{DWBA} \\
&= \sum_{j_B j_X} (C^B_{Aal_B j_B})^2 (C^X_{Yal_X j_X})^2 \left[\frac{(d\sigma/d\Omega)_{DWBA}}{b^2_{Aal_B j_B} \, b^2_{Yal_X j_X}}\right],
\end{aligned} \tag{4.47}
$$

where $X = Y + a$, $B = A + a$ and a is the transferred particle.

Since Eq. (4.44) implies $\left(\dfrac{d\sigma}{d\Omega}\right)_{DWBA} \propto b^2_{Aal_B j_B} \, b^2_{Yal_X j_X}$ for peripheral reactions [Mu01], the dependence of the DWBA cross-section on the single-particle ANC is canceled out in Eq. (4.47). The single-particle ANC can be numerically calculated from the bound state wave function and the Whittaker function. As a result, the ANC's are the only fitting parameters when the experimental and the DWBA cross sections are obtained.

The ANC from a proton transfer reaction can be used to calculate its direct proton capture rates at astrophysical energies, which is very important in the hydrogen burning

process. The proton capture reaction cross section for the reaction $A + p \rightarrow B + \gamma$ is given by [Ga02]

$$\sigma^{DC} = \lambda \left| \left\langle I^B_{Ap}(\mathbf{r}) \left| \hat{O}(\mathbf{r}) \right| \psi_i^{(+)}(\mathbf{r}) \right\rangle \right|^2 ,$$ (4.48)

where λ contains kinematic factors, I^B_{Ap} is the overlap function for $B = A + p$, $\hat{O}$ is the electromagnetic transition operator, and $\psi_i^{(+)}$ is the scattering wave in the incident channel. Assuming only one l_B for simplicity, the total direct capture (DC) reaction cross section is given by [Mu97, Mu02]

$$\sigma^{DC} = \sum_{j_B} (C^B_{Apl_B j_B})^2 \frac{\sigma^{DC}_{l_B j_B}}{b^2_{Apl_B j_B}} .$$ (4.49)

Consequently, this relationship allows us to calculate the direct proton capture reaction rates by using the ANC's. This ANC approach has an advantage over the direct measurement. Proton capture reactions have very low cross sections that have been very difficult to measure, and have large uncertainties. However, the ANC's are readily obtained from proton transfer reactions whose cross sections are orders of magnitude higher than direct capture.
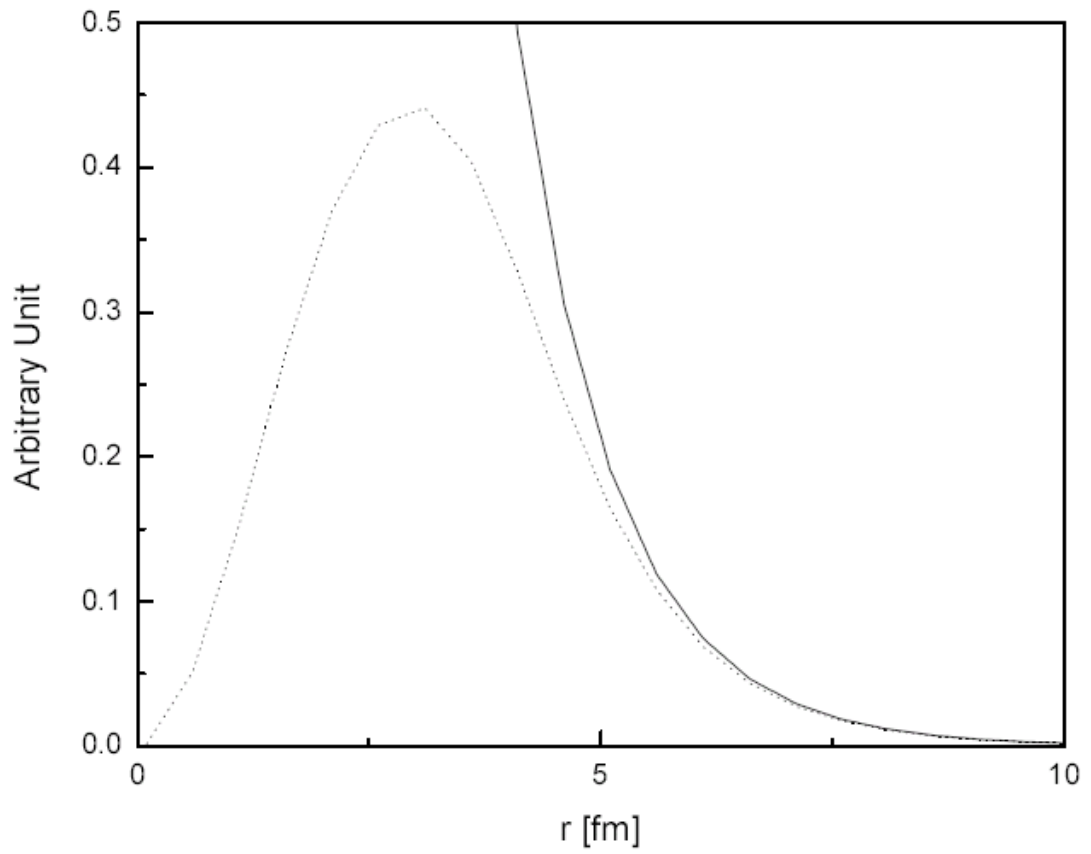
Figure 4.4 The single-particle radial wave function (dotted line) of ^{12}N (^{11}C core + single proton), and the Whittaker function (solid line). The asymptotic behavior of the wave function at large distance is described by the Whittaker function, and the single particle ANC.

CHAPTER 5
Study of the $^{11}C(p,\gamma)$ reaction via the indirect $d(^{11}C,^{12}N)n$ transfer reaction

5.1 Introduction

The $^{11}C(p,\gamma)^{12}N$ reaction is believed to be an important branch point in supermassive low-metallicity stars because it can produce CNO seed nuclei before the traditional triple-alpha (3α) process turns on. When a star consumes all its pp-chain fuel, and gravitational contraction becomes more dominant than outward thermal expansion, the 3α process turns on too late to prevent the star from collapsing to a black hole. Fuller et.al. [Fu86] showed that the existence of even a small amount of CNO seed nuclei prior to the helium burning stage could slow down the process of collapse and change the destiny of the star. Wiescher et.al. [Wi89] suggested several reaction sequences ("the hot pp-chain"), which lead to the formation of ^{12}C, instead of the traditional 3α process. These include the sequences $^7Be(\alpha,\gamma)^{11}C(p,\gamma)^{12}N(e^+\nu)^{12}C$ and $^8B(\alpha,p)^{11}C(p,\gamma)^{12}N(e^+\nu)^{12}C$. Sequences which involve ^{11}C production could be more efficient ways for ^{12}C formation, bypassing the slow 3α reaction, so that the $^{11}C(p,\gamma)^{12}N$ reaction rate and its astrophysical S-factor become of interest.

A GANIL experiment using Coulomb breakup of ^{12}N has shown that direct capture of protons by ^{11}C nuclei is the dominant mechanism and that proton capture through the first two resonance states in ^{12}N becomes less important in the temperature region below $0.3T_9$ [Le95]. The $^{11}C(p,\gamma)$ radiative capture reaction scheme is shown in Figure 5.1. The

Asymptotic Normalization Coefficient (ANC) method [Mu01, Ga01] for determining the direct capture component has been employed using the $^{14}N(^{11}C,^{12}N)^{13}C$ reaction at Texas A&M [Ta03], and the $d(^{11}C,^{12}N)n$ reaction at Beijing [Li03]. These two experiments agreed on two conclusions: 1) the astrophysical S-factor and reaction rate based on the extracted ANC values are much higher than were theoretically predicted, and 2) the direct proton capture of ^{11}C leading to the ^{12}N ground state is more important than resonance capture in the temperature region of interest ($< 0.3T_9$). However, the extracted ANC values differ from one another by 50%, and the $d(^{11}C,^{12}N)n$ experiment was limited by low statistics, so that its experimental ANC value, $(C_{eff})^2 = 2.86 \pm 0.91\, fm^{-1}$, has a large uncertainty [Li03].

5.2 Experiment: The $d(^{11}C,^{12}N)n$ Reaction

The BEARS facility at LBNL's 88-inch cyclotron provides several proton-rich radioactive ion beams for studies of exotic nuclei and nuclear astrophysics [Gu05, Pe06]. Among its radioactive ion beams, ^{11}C ($T_{1/2}$ = 20 min.) and ^{14}O ($T_{1/2}$ = 71 sec.) have been used to investigate several nuclear reactions. ^{11}C is produced via $^{14}N(p,\alpha)$ reactions by bombarding 40 μA of 10 MeV protons from LBNL's Life Sciences Division's medical cyclotron onto a nitrogen gas target, which are then transferred in the form of carbon dioxide ($^{11}CO_2$) 350 meters via a capillary line to the 88-inch cyclotron for injection into its Advanced Electron Cyclotron Resonance ion source [Po00, Po03, Gu05].

A 300 MeV $^{22}Ne^{8+}$ pilot beam was used to tune the cyclotron and beam line optics for Cave 0-2 prior to $^{11}C^{4+}$ beam tuning, and then the beam optics was first set to focus a

$^{11}\text{B}^{4+}$ beam whose cyclotron frequency is very close to that of $^{11}\text{C}^{4+}$ (the cyclotron frequency difference is only 1.4 kHz). Finally, a $^{11}\text{C}^{4+}$ beam was accelerated and stripped to its 6+ charge state by using a stripper foil (204 μg/cm^2 Al foil) in order to eliminate ^{11}B contamination. The average beam intensity of the 150 MeV ^{11}C beam on the target was about 6×10^5 ions/sec. The typical ^{11}C beam energy spread at 0° without a target was 1.18 MeV FWHM.

Figure 5.2 (a) shows the experimental setup for the d(^{11}C,^{12}N)n reaction. The focused ^{11}C beam passes through a series of Ta collimators, and impinges on 2.22 mg/cm^2 CD$_2$ target (deuterated polyethylene). Emitted ^{12}N nuclei from the d(^{11}C,^{12}N)n reaction were measured in a detector telescope, located 65 cm away from the target. This detector telescope is composed of a rectangular 7-strip ΔE (60 μm) and E (1 mm) silicon detectors with a cooling system. A trapezoid shaped collimator in front of the detector telescope was necessary to define the angles of each detector strip as shown in Figure 5.2 (b). As a result, it was possible for us to measure the forward (0° < $\theta_{c.m.}$ < 90°) and backward (90° < $\theta_{c.m.}$ < 180°) ^{12}N peaks at seven different laboratory angles. The laboratory angles of the 7 strips are 1.2, 2.0, 2.8, 3.7, 4.5, 5.3, and 6.2 degrees, from strip 1 to strip 7, respectively: These laboratory angles correspond to the c.m. angles of 10.9 (119.0), 18.9 (134.1), 27.1 (143.5), 35.9 (151.4), 45.4 (158.5), 56.5 (165.1), and 71.5 (171.4) degrees for the forward (backward) peaks, respectively. An additional single Si detector (1 mm) was located at 0° to measure the ^{11}C beam intensity. A typical two-dimensional ΔE-E$_{total}$ spectrum is shown in Figure 5.3 (a), and a $^{12}\text{N}_{g.s.}$ forward peak is clearly observed above the scattered ^{11}C. Figure 5.3 (b) shows the gated ^{12}N spectrum.

In order to calibrate the whole detection system, the $d(^{12}C,^{13}N)n$ experiment was performed with the same setup. The $d(^{12}C,^{13}N)n$ angular distribution is shown in Figure 5.4. This reaction also allowed us to compare our experimental results with the $^{12}C(d,n)^{13}N_{g.s.}$ reaction at 25 MeV [Ka86]: a 25 MeV deuteron beam on a ^{12}C target ($E_{c.m.}$= 21.41 MeV) in conventional kinematics is nearly equivalent to an 150 MeV ^{11}C beam on a deuteron target ($E_{c.m.}$= 21.56 MeV). Our cross section turned out to be somewhat lower than that of the previous study, but the difference is less than 3% at the smallest c.m. angle ($\theta_{cm} = 10.9°$). Three theoretical angular distributions are also shown in Figure 5.4, as discussed in section 5.3. Our experimental data are also in good agreement with the theoretical predictions within a 5 % difference at the smaller c.m. angles.

5.3 Data Analysis and Results

The angular distribution of the $d(^{11}C,^{12}N)n$ reaction was obtained from the measured ^{12}N peaks and is shown in Figure 5.5. Although the experimental setup was designed to cover emitted ^{12}N nuclei from 8° to 174° c.m., the data at angles beyond 72° c.m. had to be excluded because of their poor statistics. The experimental angular distribution was then compared with theoretical predictions. For the DWBA calculation, three sets of global optical model parameters for the $d(^{11}C,^{12}N)n$ reaction were obtained from the literature [Wa69, Ha71, Da80] (since ^{11}C optical model parameters were not available). These parameter sets for the $d(^{11}C,^{12}N)n$ reaction are given in Table 5.1. (Parameter Set III differs from Set I only by its spin-orbit potentials.) The DWBA analysis with these

parameter sets was first compared with our d(^{12}C,^{13}N)n data (parameter sets adjusted to describe the d(^{12}C,^{13}N)n reaction). The calculated d(^{12}C,^{12}N)n angular distributions shown in Figure 5.4 are in good agreement with our experimental results, and the ^{12}C(d,n)^{13}N study [Ka86]. The angular distributions that resulted from these parameter sets start to diverge as the c.m. angle increases, but the differences at smaller angles remained less than 3% (see Figure 5.4). For the optical model parameter sets, the adiabatic approximation method was also taken into account in order to include the break-up effect of the loosely bound deuteron [Ha71, Jo72, Ka86]. Then, these parameter sets were applied to the d(^{11}C,^{12}N)n reaction experimental data. An averaged DWBA cross section from these three sets is shown in Figure 5.5. The overall shape of the averaged angular distribution successfully describes the experimental result at these forward angles.

We now wish to extract the ANC from the transfer reaction data, and the ^{12}N→^{11}C+p ANC was deduced from the following equation.

$$
\begin{aligned}
\left(\frac{d\sigma}{d\Omega}\right)_{\exp} &= \left(\frac{C^d}{b^d}\right)^2 \times \left[\left(\frac{C^{^{12}N}_{p1/2}}{b^{^{12}N}_{p1/2}}\right)^2 \times \left(\frac{d\sigma_{p1/2}}{d\Omega}\right)_{DWBA} + \left(\frac{C^{^{12}N}_{p3/2}}{b^{^{12}N}_{p3/2}}\right)^2 \times \left(\frac{d\sigma_{p3/2}}{d\Omega}\right)_{DWBA}\right] \\
&= \left(\frac{C^d}{b^d}\right)^2 \times \left(C^{^{12}N}_{p1/2}\right)^2 \times \left[\frac{\left(\frac{d\sigma_{p1/2}}{d\Omega}\right)_{DWBA}}{\left(b^{^{12}N}_{p1/2}\right)^2} + \left(\frac{C^{^{12}N}_{p3/2}}{C^{^{12}N}_{p1/2}}\right)^2 \times \frac{\left(\frac{d\sigma_{p3/2}}{d\Omega}\right)_{DWBA}}{\left(b^{^{12}N}_{p3/2}\right)^2}\right]
\end{aligned} \qquad (5.1)
$$

This equation is Eq. (4.47) derived above, now modified for the specific d(^{11}C,^{12}N)n reaction: in Eq. (5.1), C_{lj} and b_{lj} represent the asymptotic normalization coefficient and single particle ANC of the transferred proton with the orbital angular momentum l and the total angular momentum j, respectively. The ANC's of $d \to p+n$, $(C^d)^2$ is known

to be 0.76 fm^{-1} [Bl77], and the ratio of $\left(C_{p3/2}^{^{12}N}\right)^2$ to $\left(C_{p1/2}^{^{12}N}\right)^2$ is 0.17, which is obtained

from the average value in a recent shell model calculation [Ti03a]. The DWBA cross

sections are calculated by the zero-range DWUCK4 code with a reaction normalization

coefficient of $D_o^2 = 1.55 \times 10^4 MeV \cdot fm^3$ [Sa83, Ku93, Im01], and the average of the

three DWBA cross sections is compared with the experimental result. Given all this

available information, the DWBA cross section is then normalized to the experimental

result, adjusting $C_{p_{1/2}}^{^{12}N}$ as a fitting parameter. The extracted ANC is found to be

$\left(C_{p_{1/2}}^{^{12}N}\right)^2 = 1.56 \pm 0.23\, fm^{-1}$, and the ratio of $p_{1/2}$ to $p_{3/2}$ leads to $\left(C_{p_{3/2}}^{^{12}N}\right)^2 = 0.26 \pm 0.05\, fm^{-1}$.

Finally, the total effective $^{12}N \rightarrow ^{11}C + p$ ANC is obtained to be

$\left(C_{eff}^{^{12}N}\right)^2 = \left(C_{p_{1/2}}^{^{12}N}\right)^2 + \left(C_{p_{3/2}}^{^{12}N}\right)^2 = 1.83 \pm 0.27\, fm^{-1}$. The uncertainty mainly comes from the

systematic errors in the experimental (statistics) and the theoretical DWBA cross section

(optical potential models).

The extracted ANC is then used to calculate the astrophysical S-factor and stellar

reaction rate of the $^{11}C(p,\gamma)$ reaction. The direct capture cross section to the ^{12}N ground

state is calculated by the RADCAP code [Be03], and the Breit-Wigner resonance formula

is used for the population of the 2^+ (E$_x$=0.960 MeV) and 2^- (E$_x$=1.190 MeV) resonance

states in ^{12}N. For the 2^+ state, only an upper limit of 20 keV has been established for the

Γ_p [Aj90], but suggested values of 5.5 keV [Le95] and 2.6 meV [Wi89, Le95] have been

used for Γ_p and Γ_γ, respectively, in this thesis. A Γ_p of 118 keV [Aj90] and Γ_γ of

13.0 meV [Mi02] were adopted for the 2^- state.

The calculated astrophysical S-factor is shown in Figure 5.6, including an interference term between the direct capture (DC) and the broad 2⁻ resonance (R) state, which is expressed by

$$S(E) = S_{DC}(E) + S_R(E) + 2[S_{DC}(E)S_R(E)]^{1/2}\cos[\delta_R(E)], \qquad (5.2)$$

where $\delta_R(E) = \arctan\dfrac{\Gamma_R}{2(E - E_R)}$ is the resonance phase shift [Bu88]. The S-factor at zero energy is found to be $S(0) = 0.097 \pm 0.020\,\text{keVb}$ in this work. Given the direct and resonance capture cross sections, the $^{11}\text{C}(p, \gamma)$ reaction rate as a function of stellar temperature can also be calculated, and is shown in Figure 5.7.

5.4 Discussion and Summary

The extracted $^{12}\text{N} \rightarrow {}^{11}\text{C}+\text{p}$ ANC of $1.83 \pm 0.27\,fm^{-1}$ in this work is less than the $2.43 \pm 0.77\,fm^{-1}$ from the same transfer reaction study of Ref. [Li03] (but the measurements agree within error bars). However, our result is improved by its better statistics (due to our higher ^{11}C beam intensity), and shows good agreement with the reported value of $\left(C_{\text{eff}}^{^{12}N}\right)^2 = 1.73 \pm 0.25\,fm^{-1}$ from the $^{14}\text{N}(^{11}\text{C}, {}^{12}\text{N})^{13}\text{C}$ reaction [Ta03]. This shows that the ANC can be experimentally obtained with consistent nuclear properties regardless of the experimental reaction scheme. In addition, a study [Ti03b] has reported that the ^{12}N ANC could be estimated based on known information for its mirror nucleus, ^{12}B. They developed a relationship between the proton and neutron squared ANC's in the two mirror nuclei, and then obtained a ratio of 1.37 between ^{12}N and ^{12}B from theoretical potential model calculations. The experimental ^{12}B ANC is

$$\left(C_{\exp}^{^{12}B}\right)^2 = \left(C_{n1/2}^{^{12}B}\right)^2 + \left(C_{n3/2}^{^{12}B}\right)^2 = 1.35\, fm^{-1}$$ from a d(^{11}B,^{12}B)p reaction study [Li01]. This implies that the effective ^{12}N ANC value is expected to be $1.84\, fm^{-1}$, which is in accordance with our experimental result.

The astrophysical S-factor at zero energy, $S(0)$, from our calculation turned out to be about two times larger than that from the Coulomb breakup experiment [Le95], but agrees with those from ANC method studies. The direct capture reaction dominantly contributes to the total S-factor in the energy region of astrophysical interest. The interference term increased the S-factor slightly in the low energy region as shown in Figure 5.6.

In the temperature region of $0.2 < T_9 < 0.4$, the reaction rate is dominated by the direct and the 2^- resonance captures, while the contribution from the 2^+ state is less important (see Figure 5.7). As a result, we can confirm 1) that the major contribution to the ^{11}C(p,γ) reaction rate comes from the direct capture reaction as was concluded in previous studies, and 2) that the ^{11}C(p,γ) reaction rate appears to be higher than the previous estimate [Ta03, Li03]. This result confirms that the ^{3}He(α,γ)^{7}Be(α,γ)^{11}C(p,γ)^{12}N reaction sequence is also an important path in producing CNO nuclei in low-metalicity supermassive stars.

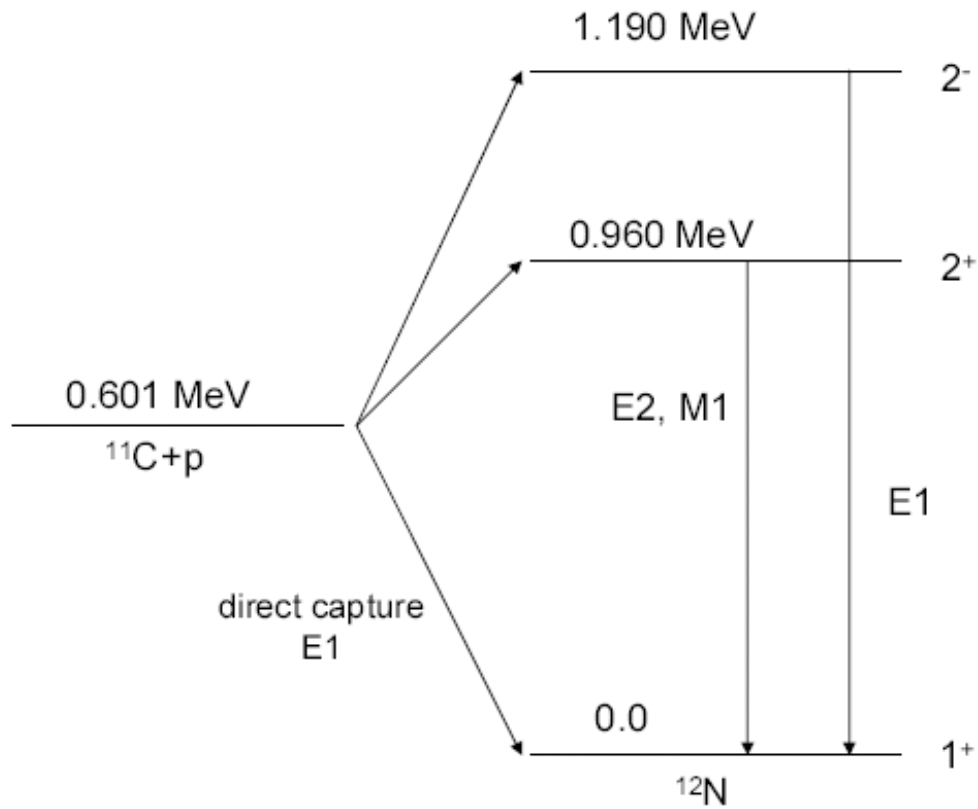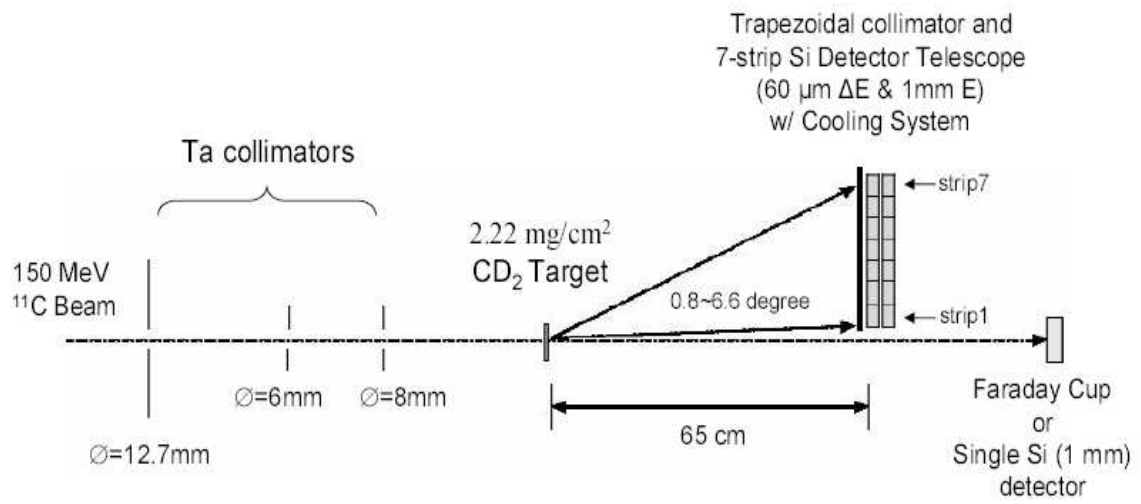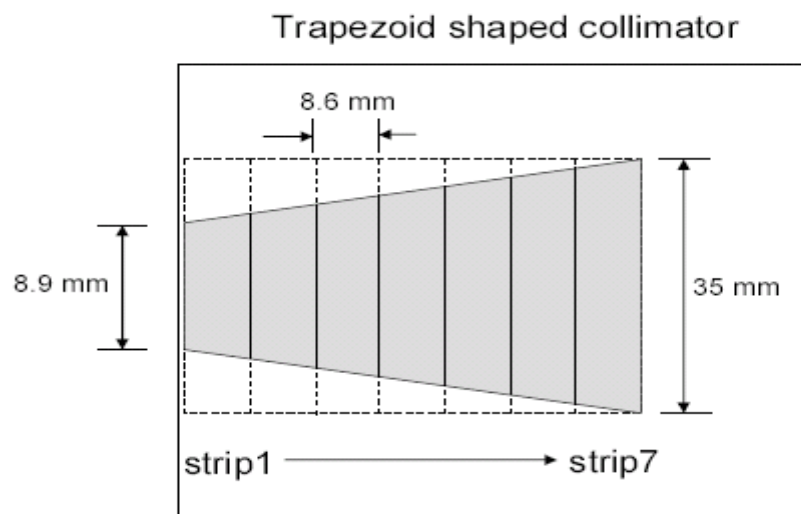Figure 5.1 The ^{11}C(p,γ) radiative capture reaction scheme. Resonant captures through the 2$^+$ and 2$^-$ states in ^{12}N are also shown along with direct capture to the ^{12}N$_{g.s.}$ Note that all excited states in ^{12}N are proton unbound.

(a)

(b)

Figure 5..2 (a) The d(^{11}C,^{12}N)n reaction experimental setup. (b) Front view of the 7-strip Si detector through a trapezoidal collimator
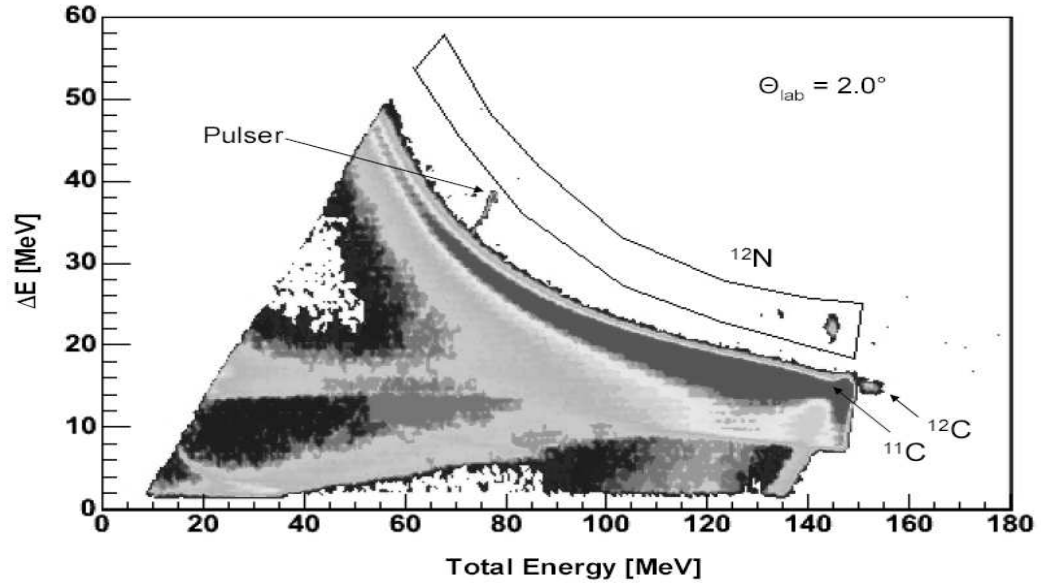
(a)
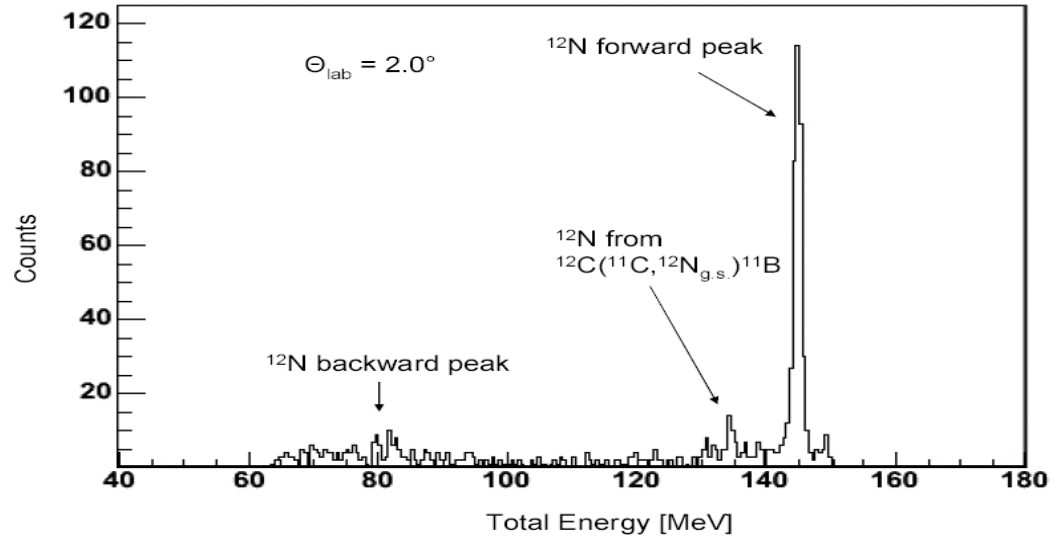
(b)

Figure 5.3 (a) A two-dimensional particle identification spectrum from ΔE-E_{total} coincidences at the second strip. The ^{12}N gate is shown above the scattered ^{11}C beam. Note that ^{12}C also appears from the d(^{11}C,^{12}C)p reaction. (b) A one-dimensional spectrum inside the ^{12}N gate. A ^{12}N$_{g.s.}$ forward peak is clearly observed along with background from the ^{12}C(^{11}C,^{12}N$_{g.s.}$)^{11}B reaction.
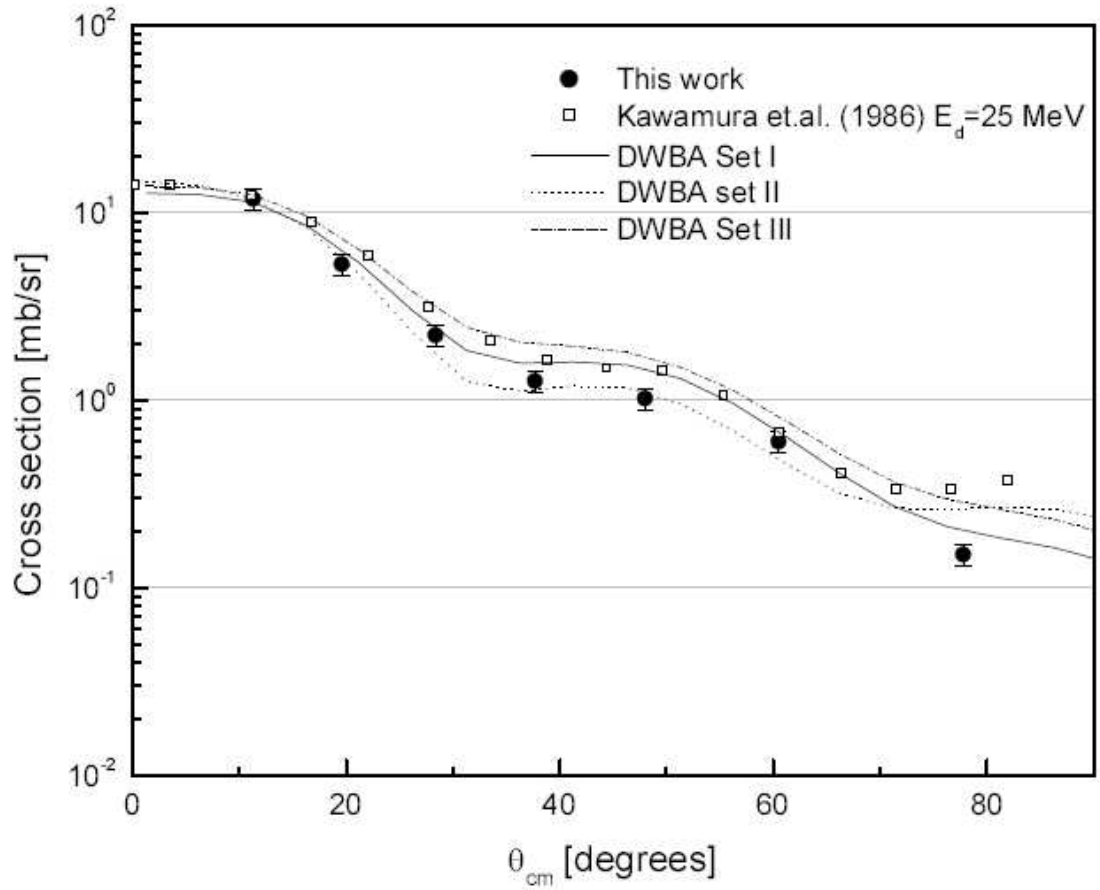
Figure 5.4 The d(^{12}C,^{13}N)n reaction angular distribution. Our experimental results are compared to those from a previous study of ^{12}C(d,n)^{13}N (see text). Error bars are shown (this work) or are within the open rectangles. Three different theoretical angular distributions (DWBA) are also shown.
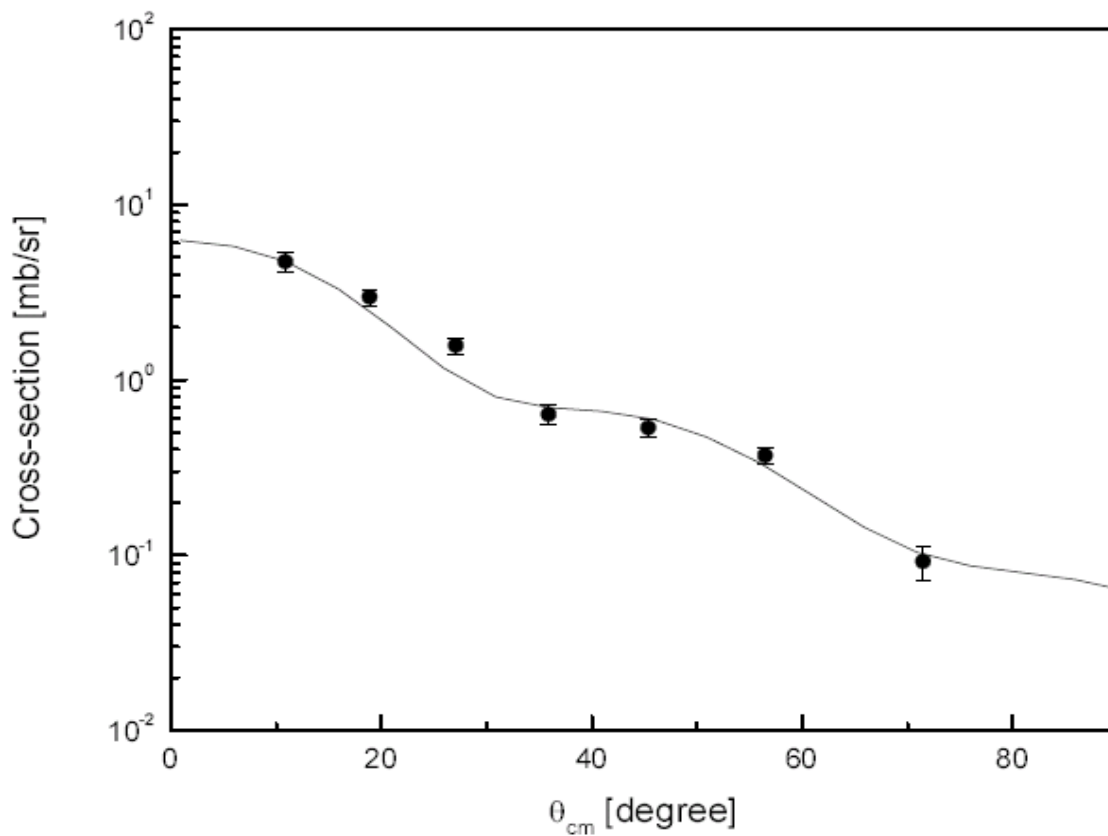
Figure 5.5 The d(^{11}C,^{12}N)n reaction angular distribution. Black squares are our experimental results, and the solid line represents averaged DWBA cross sections based on three different optical model parameter sets (see text).
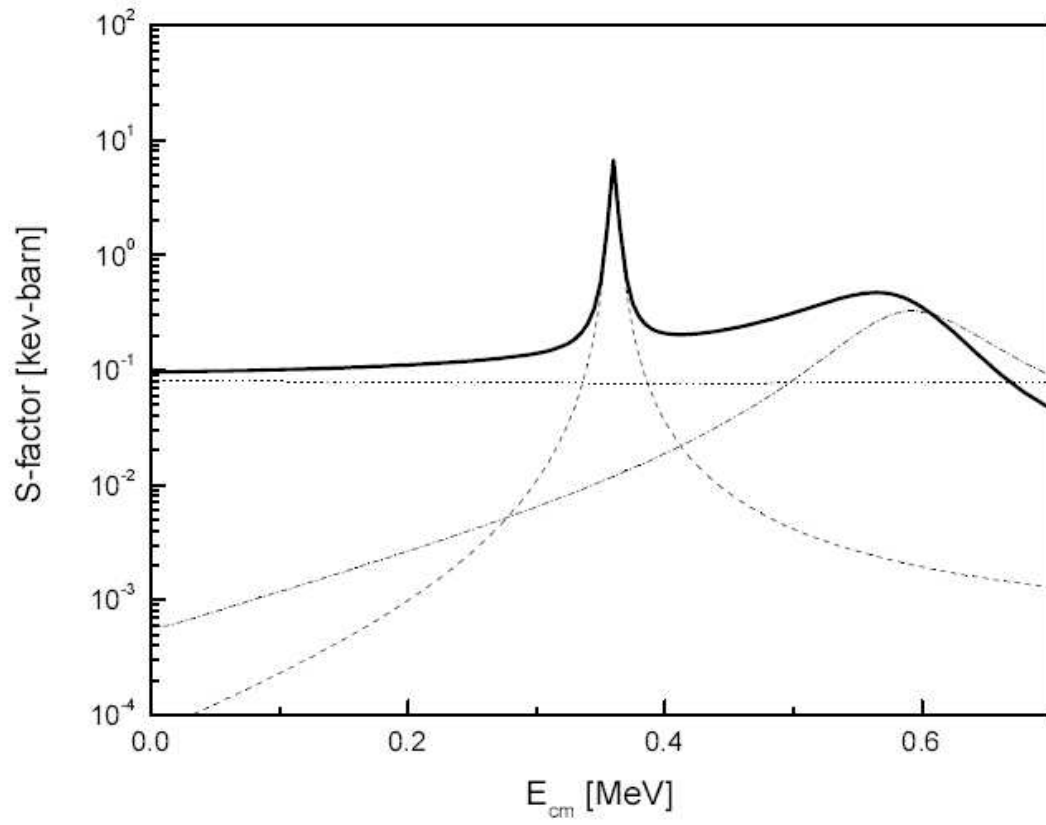
Figure 5.6 The calculated ^{11}C(p,γ) astrophysical S-factor, based on the extracted ANC value. The dotted line represents the S-factor from direct capture. The dashed line is the contribution from the 2^+ state, and the dash-dotted line from the 2^- state in ^{12}N. The solid line is the total S-factor, including the interference term between direct capture and the 2^- state.
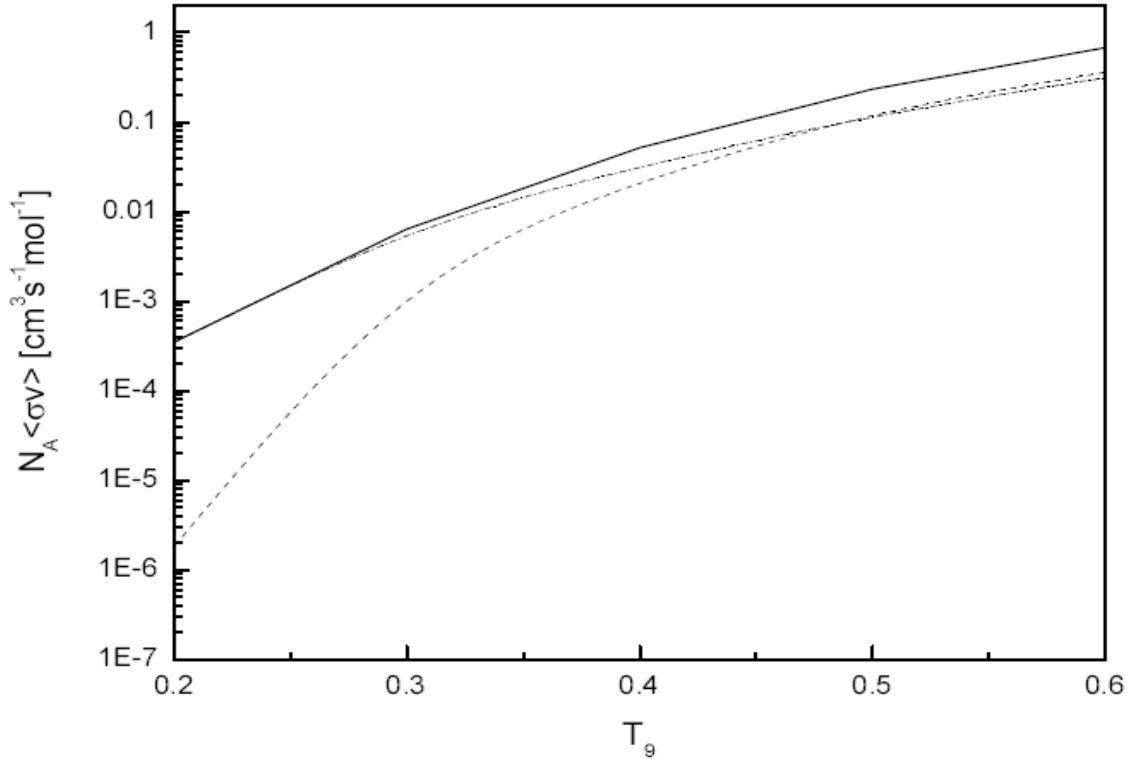
Figure 5.7 ^{11}C(p, γ) stellar reaction rate. The dashed line shows the contribution of the

narrow 2^+ state, and the dash-dotted line is the combination of the direct capture and the

broad 2^- state. The solid line represents the total ^{11}C(p, γ) stellar reaction rate as a

function of stellar temperature T_9 (10^9 K). It clearly shows that the sum of the direct

capture and the resonant capture through the 2^- state dominates in the low temperature

region (see text).

Table 5.1 Optical model parameters for the d(^{11}C,^{12}N)n reaction. (V and W are expressed in MeV, and r and a in fm.)[*].

Set		V_r	W_i	W_D	V_{so}	r_o	a_o	r_i	a_i	r_{so}	a_{so}	r_c
I :	d [a,b]	114.2	0.0	13.68	3.0	1.14	0.61	1.14	0.54	1.14	0.61	1.14
	n [a]	58.1	0.0	9.98	26.0	1.13	0.57	1.13	0.50	1.13	0.57	1.13
II :	d [c]	83.8	0.93	11.98	6.54	1.17	0.76	1.33	0.53	1.07	0.66	1.30
	n [a]	58.1	0.0	9.98	11.0	1.13	0.57	1.13	0.50	1.13	0.57	1.13
III :	d [a,b]	114.2	0.0	13.68	11.0	1.14	0.61	1.14	0.54	1.14	0.61	1.14
	n [a]	58.1	0.0	9.98	11.0	1.13	0.57	1.13	0.50	1.13	0.57	1.13

a. From Ref. [Wa69] and our d(^{12}C,^{13}N)n results.

b. From Ref. [Ha71]

c. From Ref. [Da80]

---

[*] The potential $V(r)$ in the DWUCK4 code is given by

$$V(r) = -V_r f(r,r_o,a_o) - iW_i f(r,r_i,a_i) + 4iW_D \frac{d}{dr} f(r,r_i,a_i)$$

$$+ V_{SO} \left(\frac{\hbar}{m_\pi c} \right) \frac{1}{r} \frac{d}{dr} f(r,r_{SO},a_{SO}) \mathbf{L} \cdot \mathbf{s} + V_C(r)$$

where $f(r,r_j,a_j) = \dfrac{1}{1 + \exp\left(\dfrac{r - r_j M_{target}^{1/3}}{a_j} \right)}$ and $V_C(r)$ is the Coulomb potential.

CHAPTER 6

Study of Low-lying Resonant States in ^{16}F using an ^{15}O Radioactive Ion Beam

6.1 Introduction

Among the nuclei in the A=16, T=1 isobaric triad, many states in ^{16}N and ^{16}O have been well established, but less has been reported on ^{16}F. Four states of ^{16}F below 1 MeV have been identified experimentally, and their energies are currently known to an accuracy of 4-6 keV (the next known state of ^{16}F lies at 3.76 MeV) [Ti93]. Experimental studies with stable beams have also established spin-parity values for these low-lying states, but only upper limits or rough estimates of their level widths have been reported. The main difficulty in characterizing ^{16}F has been that it can be broadly studied by relatively few reactions, primarily ^{14}N(^{3}He,n) [Za65, Bo73, Ot76], ^{16}O(^{3}He,t) [Pe65, Na77, St84, Fu02], ^{16}O(p,n) [Mo71, Fa82, Or82, Oh87, Ma97], and ^{19}F(^{3}He, ^{6}He) [Na77].

All the states in ^{16}F are unbound to ^{15}O+p. The spins and parities of the low-lying states have been found to be 0^-, 1^-, 2^-, and 3^- in ascending order in energy, and are believed to have ^{15}O core-single proton configurations, namely $1p_{1/2}^{-1}$ $2s_{1/2}$ for the 0^-, 1^- states and $1p_{1/2}^{-1}$ $1d_{5/2}$ for the 2^-, 3^- states [Fa82, St84]. However, the variation in the $1d_{5/2}$-$2s_{1/2}$ energy level difference across the members of the A=16, T=1 isobaric triad [Fo95, Og99] made initial ^{16}F spin assignments uncertain [Za65, Ot76] since ^{16}N showed J^π = 2^-, 0^-, 3^-, 1^- for the four levels in ascending energy order while J^π = 0^-, 2^-, 1^-, 3^- arose in ^{16}O, as is shown in Figure 6.1.

A recently developed ^{15}O radioactive ion beam from the BEARS facility has been used to study the structure of ^{16}F using ^{15}O+p elastic resonance scattering and the Thick Target Inverse Kinematics (TTIK) method on a polyethylene target [Ar90, De92]. Of particular interest is establishing the level widths of the low-lying ^{16}F states, which can be compared to theoretical calculation for this proton unbound nucleus.

6.2 Experiment

Production of ^{15}O beams ($T_{1/2}$= 122 sec) with BEARS is described in Chapter 2, and this particular experiment was performed in Cave 0-2 at the 88-inch cyclotron. To set up the beam optics for Cave 0-2 and eliminate the ^{15}N component of the beam, a 160 MeV ^{20}Ne^{8+} beam was initially used as a pilot beam; then a weak 120 MeV ^{15}N beam was tuned into the experimental area, since the ^{15}N^{6+} accelerating frequency is very close to that of the ^{20}Ne^{8+}. Next, the ^{15}N beam was fully stripped to its 7+ charge state by passing it through a thin aluminum stripper foil placed before an analysis magnet. The subsequent beam optics was then adjusted to focus the ^{15}N^{7+} beam on the target. These adjustments were then changed to obtain ^{15}O^{8+} from an accelerated and stripped ^{15}O^{6+} beam. Finally, the cyclotron was carefully tuned to maximize a focused 120 MeV ^{15}O^{8+} beam on the target position, eliminating ^{15}N contamination as much as was possible. However, the cyclotron frequency difference between ^{15}N^{6+} and ^{15}O^{6+} is so small (1.2 kHz) that a residual amount of ^{15}N contamination was still observed in the low energy region of the ^{15}O spectrum. The measured amount of ^{15}N contamination of the ^{15}O beam was less than

2 % throughout the experiment. The ^{15}O beam profile measured at 0° in the laboratory using a single silicon detector (see below) is shown in Figure 6.2.

Figure 6.3 shows the last stage of the experimental setup. At the beginning of the experiment, the ^{15}O beam was counted at 0° with a single silicon detector (1,000 μm), and scattered ^{15}O beam from a thin gold foil was measured simultaneously by a ΔE-E monitor telescope (25 μm and 300 μm, respectively) placed at 20° to the beam axis. The ratio between these two measurements allowed us to calculate that the average beam intensity of ^{15}O impinging on the target was 4.5×10^4 pps. The beam energy spread was measured to be 1.66 MeV FWHM at 0° after going through the aluminum stripper foil and the gold scattering foil (see Figure 6.3).

For the ^{15}O+p experiment, the 120 MeV ^{15}O beam[†] was slowed down by a 3.81 μm Ni degrader, and completely stopped in a thick 200 μm (18.4 mg/cm^2) CH$_2$ target. The thickness of Ni degrader was chosen to stop the ^{15}O beam very close to the end of the target, minimizing the energy loss of emerging low energy protons within the CH$_2$ target. The main particle telescope was composed of ΔE (30 μm), E1 (700 μm), and E2 (5,000 μm) silicon detectors, located at 0° at a distance of 10.9 cm from the target. The first two detectors were thick enough to detect protons from the four low-lying resonance states in ^{16}F, and the third one permitted the detection of high energy protons of up to 7 MeV in the center-of-mass (c.m.). The total energy resolution was found to be 28 keV c.m. (FWHM) for the energy region below 3 MeV c.m., including contributions from electronic noise, detector/setup geometry [Mo66], and beam straggling [Ma00] in the CH$_2$ target.

[†] This beam energy was chosen to permit maximum ^{15}O production by extracting the 6+ charge state from the AECR ion source, which has the maximum yield.

Figure 6.4 shows a typical two-dimensional particle identification spectrum recorded during the experiment using the ΔE-E1 part of the detector telescope. The proton band is clearly shown in this figure along with a lot of β^+ counts. A gate was drawn around this proton band, and the proton spectrum inside the gate was converted into a one-dimensional excitation function. This excitation function consisted of the sum of the ΔE and E1 detectors up to 2.7 MeV c.m. (see Figure 6.4 caption) and at higher energies was the sum of the ΔE, E1 and E2 detectors (in triple coincidence). The energy calibration for the ΔE-E1 and the ΔE-E1-E2 detector system was established by using the p(^{15}N,p) reaction [Ha57, Ba59, De62, Da84] before and after the main p(^{15}O,p) measurement because the energy levels of the relevant excited states in ^{16}O are well known. The measured laboratory energy of the protons at a given laboratory angle can then be converted to center-of-mass energy by using

$$E_{c.m.} = \frac{m_p + M(^{15}O)}{4M(^{15}O)\cos^2 \vartheta_{lab}} E_{p,lab.} \, .$$

(6.1)

Finally, proton counts were converted into cross-sections without any background subtraction, so that an arbitrary cross-section unit has been used for the excitation function. The experimental cross-section, $\frac{d\sigma}{d\Omega}$, was calculated by using an energy-dependent target thickness, Δx, which is inversely proportional to the stopping power, $\frac{dE}{dx}$ [Zi03]:

$$\frac{d\sigma}{d\Omega} = \frac{R}{\rho \times \Delta x \times I \times \Delta\Omega} = \frac{R}{\rho \times \left(\Delta E \times \frac{dx}{dE} \right) \times I \times \Delta\Omega} \, ,$$

(6.2)

where R is the proton yield, ρ is the target density [atoms/cm^3], $\varDelta\Omega$ is the detector solid angle, and I is the time integrated ^{15}O beam intensity [Ku01, Te03].

Figure 6.5 shows our measured p(^{15}N,p) excitation function along with the results from the two previous ^{15}N(p,p) studies [Ba59, Da84]. The uncertainty of our energy calibration was estimated to be about ± 15 keV in the center-of-mass frame. Figure 6.6 then shows the p(^{15}O,p) excitation function up to 6.5 MeV, measured at 180° c.m. using the data from the complete detector telescope (ΔE, E1, E2) as described earlier.

6.3 Data Analysis

In this study, the level widths of the first four states in ^{16}F were the main focus of the data analysis, so that only the low energy region below 3 MeV in the center-of-mass was selected for R-matrix analysis. As shown in Figure 6.7, the first four states in ^{16}F are quite distinguishable, and the interference between potential and resonance scattering is clearly observed. In order to compare these experimental results with theory, a resonance scattering analysis code, which is based on Eq.(4.30) and Eq. (4.38) in Chapter 4 (also see Ref. [La58, Ru05] for more details), was written to calculate the theoretical excitation function. In order to perform the correct comparison with theory, background subtraction is necessary because protons from the reaction between the ^{15}O beam and ^{12}C in the CH$_2$ target may contribute to the measured proton spectrum. Due to the limited beam time, we did not measure the ^{12}C(^{15}O,p) spectrum. As a result, the earlier ^{12}C(^{14}O,p) reaction data using 120 MeV ^{14}O were used to estimate this background contribution [Gu05]. This

background proton spectrum is also shown in Figure 6.7, and the background is small in the region of the four low-lying resonances.

The J^π values of these four states are 0^-, 1^-, 2^-, and 3^- (as discussed earlier). To make the analysis simple, the 0^- and 1^- states are assumed to be pure $1p_{1/2}^{-1} 2s_{1/2}$ configurations, and only s-wave contributions to these resonances are considered. For the 2^- and 3^- states, only d-wave contributions are considered with a $1p_{1/2}^{-1} 1d_{5/2}$ configuration. Theoretical shell model calculations predict that the amplitudes of these simple configurations are well over 0.97 in these states (see Table III in Ref. [Fa82] and Table 4 in Ref. [St84]). The partial width of each combination of channel spin, s, and orbital angular momentum, ℓ, is represented as $\Gamma_{s\ell}$, which is a key parameter in the data fitting.

For the data fitting, the R-matrix calculation was convoluted with the experimental resolution function, and compared to the experimental cross section, after adding the background function discussed earlier whose shape was adopted from an earlier $^{12}C(^{14}O,p)$ experiment. All the fitting parameters in both the R-matrix analysis (E_R and $\Gamma_{s\ell}$) and the background function (a simple Gaussian function) were iterated using a minimization algorithm, MINUIT [Ja75], until the lowest chi-square per degree of freedom was obtained. This procedure was repeated, changing the initial values, upper/lower limits and step sizes of the fitting parameters, until the best χ^2 value was obtained.

A channel radius of 5 fm obtained by the conventional formula $r = 1.45 \left(A_1^{1/3} + A_2^{1/3} \right) fm$ was used in the all R-matrix calculations. Different values for the channel radius within a range from 4.5-5.5 fm were also tested, but no significant change in the results was observed. Finally, the level width and excitation energy of each

state were obtained from the average value of these fitting results; the average χ^2 value was 1.08 per degree of freedom, which varied from 0.84 to 1.27.

6.4 Results and Discussion

The experimental cross section and the R-matrix calculations are shown in Figure 6.7, where the adopted background function is also shown. The level widths and excitation energies of the four states in this study are summarized in Table I. Spin-parity assignments were not tested in this work because data were only taken at one angle, but a different order of J^{π} values such as 0^-, 2^-, 1^-, and 3^- for the first four states in ^{16}F was found to create an excitation function whose χ^2 value was unacceptable. The excitation energies of these four states were also fitting parameters, and the results are in very good agreement with the known values [Ti93]. However, no improvement in the values was possible since these values are already known quite accurately with uncertainties less than 10 keV.

The level widths in Table I obtained from the ^{15}O+p data show several different results when compared with the compiled values from the previous studies. The level widths of the 0^-, and 1^- states were reported to be 40 ± 20 keV and less than 40 keV, respectively, in Ref. [Ti93]. Our study finds that the 0^- state has a level width of 23.1 ± 2.2 keV, and that the broader 1^- state has a width of 91.1 ± 9.9 keV (about twice the compiled value). However, the ^{14}N(^{3}He,n)^{16}F data [Ot76] reported that the first two states are 1^-, and 0^- with level widths of 39 ± 20 keV, and 96 ± 20 keV, respectively (see Table I). Also note that the ^{16}O(^{3}He,tp) data [St84] reported similar results (to ours) of ~ 25 keV

75

and ~ 100 keV for the 0⁻ and 1⁻ state, respectively. The level width of the 2⁻ state is found to be 3.3 ± 0.6 keV which is much narrower than the compiled value of 40 ± 30 keV, while 14.1 ± 1.7 keV for the 3⁻ state is in good agreement with < 15 keV in Ref. [Ti93]. As reflected in the experimental results, the 0⁻ and 1⁻ states show relatively broad peaks as would be expected from s-wave scattering compared to the narrower 2⁻ and 3⁻ states from the d-wave scattering.

In order to compare these experimental level widths to theoretical expectations, the single particle width of each state, Γ_{sp}, was obtained from a potential model calculation for two different diffusion parameters, a, as is shown in Table II (also see Table III). This single particle width calculation allows us to estimate the proton partial width of each state using the equation $\Gamma_p = C^2 S \Gamma_{sp}$ if we know the single-particle spectroscopic factor, $C^2 S$. Experimental spectroscopic factors for ¹⁶N, which has the same core-single particle configuration as ¹⁶F, are available from a ¹⁵N(d,p)¹⁶N transfer reaction study [Bo72]. However, they are a factor of two less than theoretical prediction and this discrepancy has not been clearly explained (see discussion in Ref. [Bo72]). Theoretical spectroscopic factors for the analogue states in ¹⁶N [Me96] are given in Table II for comparison.

As can be seen in Table II, the widths of all four levels are close to the single particle shell model predictions with either of the two diffusion parameters. This successful single particle approach was then applied to the level shifts between the mirror nuclei. We wanted to calculate the shifts with two goals: (1) to understand how the general features of the potential affect the isotopic shift for the s-states in ¹⁶N and ¹⁶F, and (2) to obtain an additional estimate of the single particle spectroscopic factors for the s-states. The

isotopic shift of the levels depends primarily on the global radial distribution of the wave functions in the Coulomb field. It is well known [Th51, Eh51, No69] that the shift (to stronger binding) in the proton-rich nuclide is greatest for s-states due to the greater spacial extent of their wave functions.

The calculations were made with two sets of potential parameters (Table III) for the Woods-Saxon distribution, which mainly differ by two parameters. The first, the conventional calculation, had the radius parameter r_0 = 1.2 fm and the diffuseness parameter, a = 0.65 fm; the second, more diffuse potential had a smaller radius, which was compensated by a larger a = 0.75 fm. Then the well depths of the potentials were fixed by a fit to the excitation energies of the levels in ^{16}N, and the same parameters were used to calculate the excitation energies of the levels in ^{16}F. The only new factors in the calculations for ^{16}F were a small change of the reduced mass and the Coulomb potential of the uniformly charged sphere with radius parameter, r_C, of 1.2 fm. (The change of this parameter to 1.17 fm resulted in ~10 keV shift toward less binding)

The "conventional" parameters in Table III result in a ^{16}F ground state binding energy of -0.577 MeV, which is smaller than the experimental value of -0.535 MeV. We consider this disagreement as evidence of a need for a change of the parameters, which were fixed for stable nuclei [see also Go04]. Use of the diffuse potential provides 42 keV more binding than experiment for the 0$^-$ state and 58 keV more than for the 1$^-$ state (535 keV + 193 keV). In this case we can consider the differences as an indication that the spectroscopic factors of these states are less than the single particle limit. To estimate the needed changes of the spectroscopic factors, we took the ratio of the differences between the calculated and experimental level positions to the average difference between the

excitation energies of the $2s_{1/2}$ states (0^- and 1^-) and the $1d_{5/2}$ states (2^- and 3^-) in ^{16}N and ^{16}F. As a result, we obtained 0.91 for the spectroscopic factor of the 0^- state, and 0.88 for the 1^- state (see Table II).

The absolute values of the spectroscopic factors are dependent upon the excitation energies of the $1d_{5/2}$ states in our approach. These excitation energies in their turn are dependent upon electromagnetic corrections and details of their nuclear structure (one can consider mixing with the nearest $d_{3/2}$ states, for example). These corrections could be as large as 100 keV, which would result in 2% corrections to the absolute values of the spectroscopic factors. In addition, the differences in the values of the spectroscopic factors for the 0^- and 1^- states can have physical meaning. The smaller spectroscopic factor for the 1^- state can be related to a possible admixture of the $1p_{1/2}^{-1}\ 1d_{3/2}$ configuration (it is much more difficult to find a possible admixture for the $J^\pi = 0^-$).

In conclusion, the experimental data on the widths and the excitation energies of the lowest states in ^{16}F favor the more diffuse nuclear potential, as was observed earlier for the ^{15}F case [Go04]. The four low-lying states of ^{16}F manifest remarkably clear single particle structure. In this sense the population of these levels in different nuclear reactions can be used as a test of nuclear reaction theory as was proposed recently in [Mu05].
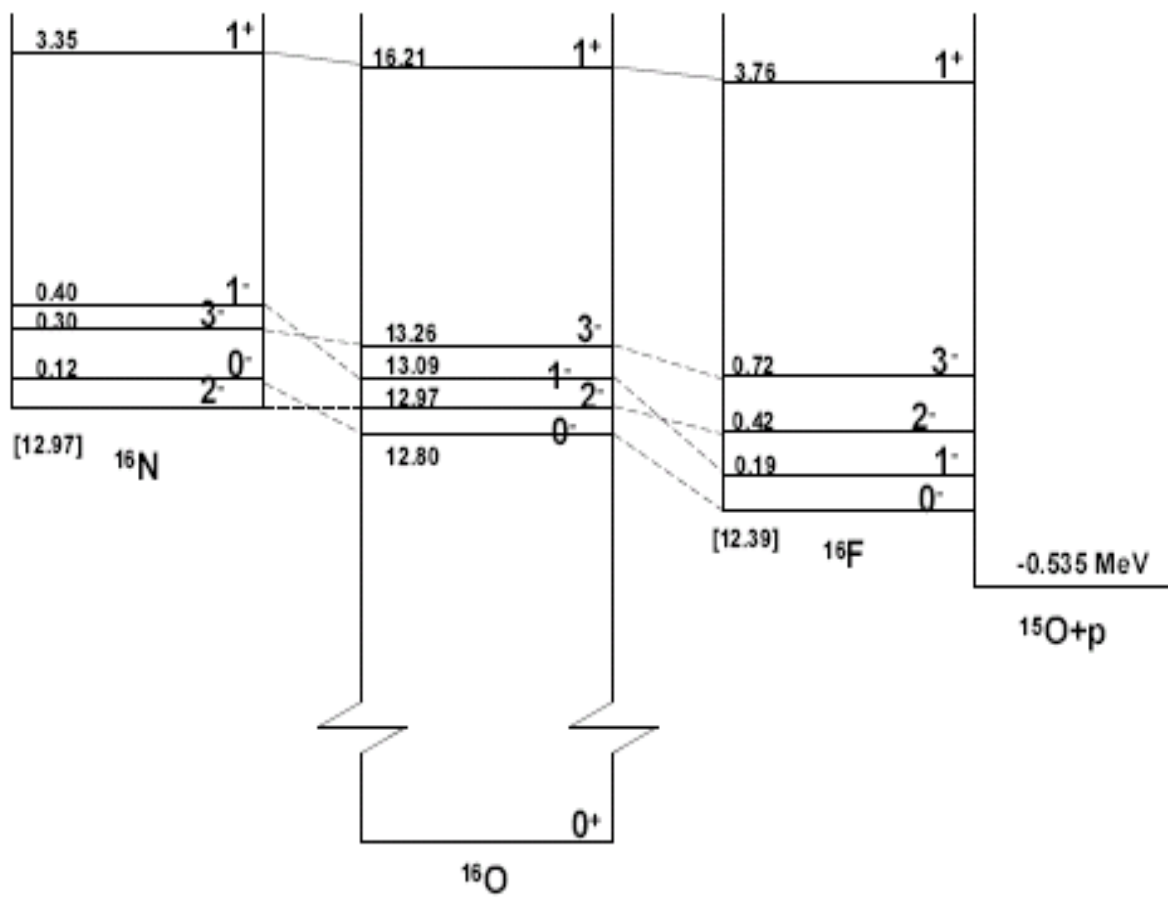
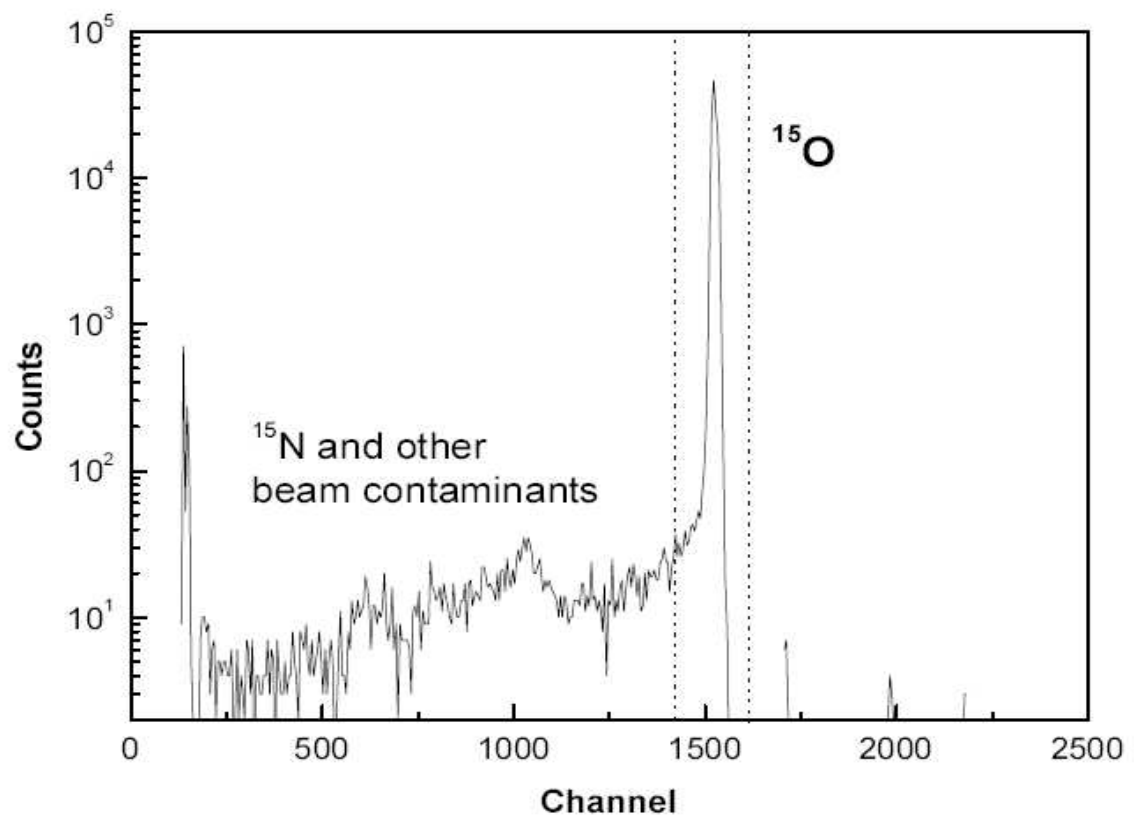Figure 6.1 An isobaric energy level diagram for the A=16, T=1 nuclear states [Ti93].

Figure 6.2 The observed ^{15}O beam profile at 0° in the laboratory without a Ni degrader

and a target. A small tail consisting of ^{15}N and other beam contaminants is observed. See

text.
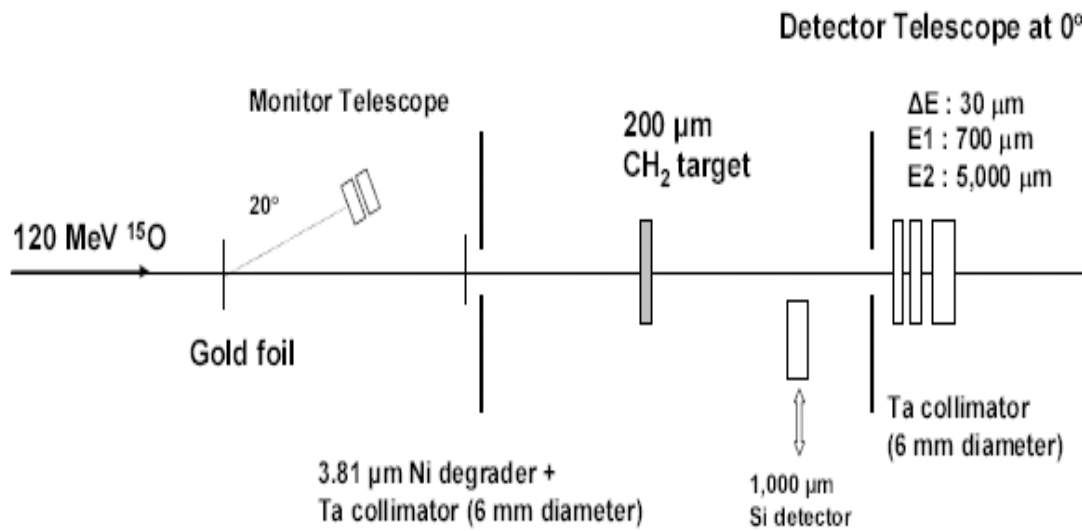
Figure 6.3 The experimental setup for the ^{15}O+p resonance scattering reaction. See text.
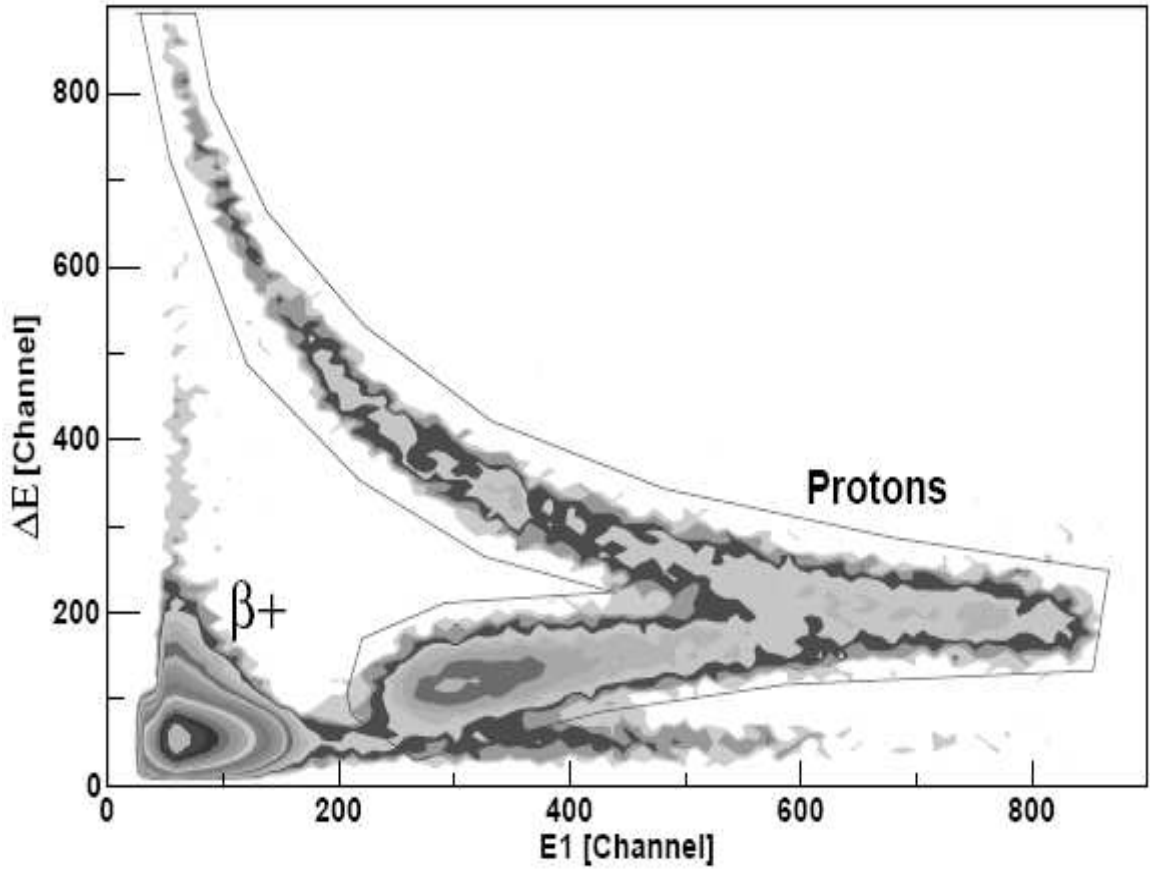
Figure 6.4 A typical two-dimensional particle identification spectrum for ΔE-E1 coincidences. Protons with energies below 2.7 MeV c.m. (around channel number 850 in E1) stopped in the ΔE-E1 detector telescope. Protons above this energy punched through the E1 detector and were also recorded in coincidence in the E2 detector. Consequently, the deposited energy in both the ΔE and the E1 detectors starts decreasing after this point, as is shown. See text.
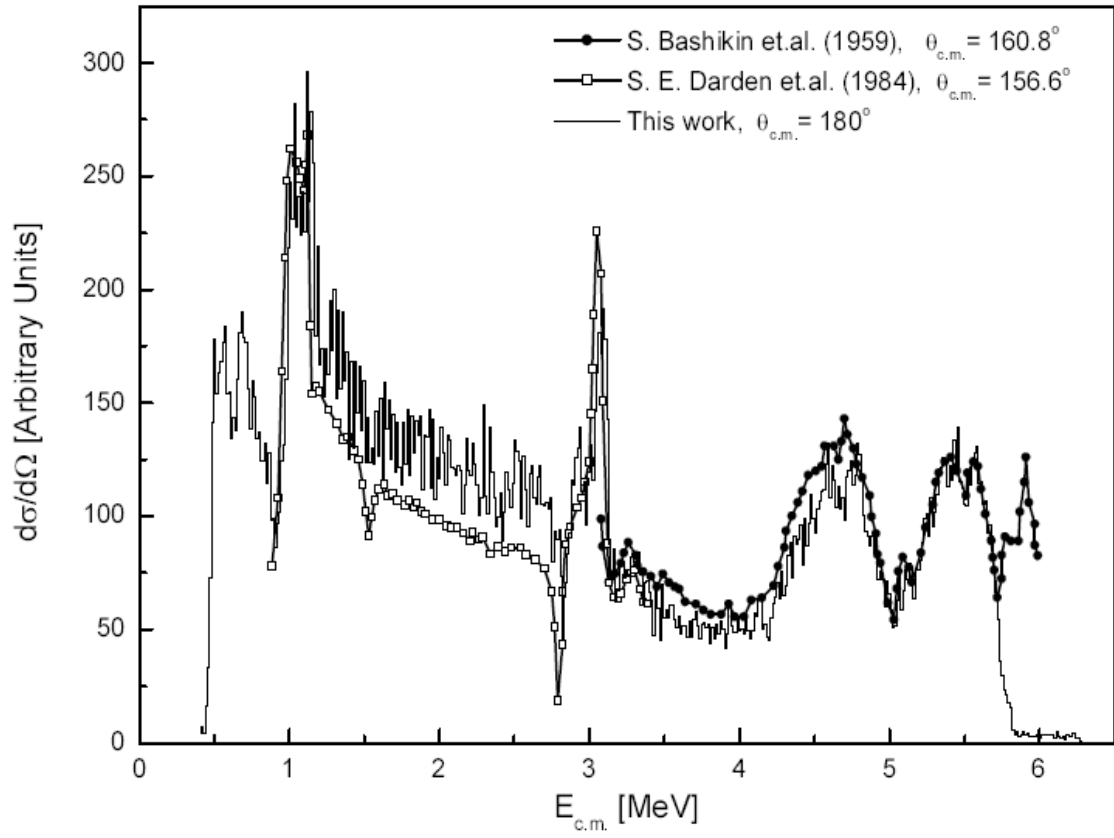
Figure 6.5 The measured ^{15}N+p excitation function at 180° c.m. without background subtraction used for the energy calibration. Experimental results from previous studies at different c.m. angles are also shown.

Figure 6.6 The measured ^{15}O+p excitation function at 180° c.m. up to 6.5 MeV c.m.

Figure 6.7 The R-matrix fit for the low-lying states in ^{16}F. The solid line represents the R-matrix calculation added to the background; the background function is shown as a dashed line. See text for details.

Table 6.1 comparison of previous experimental studies with our results for the level widths.

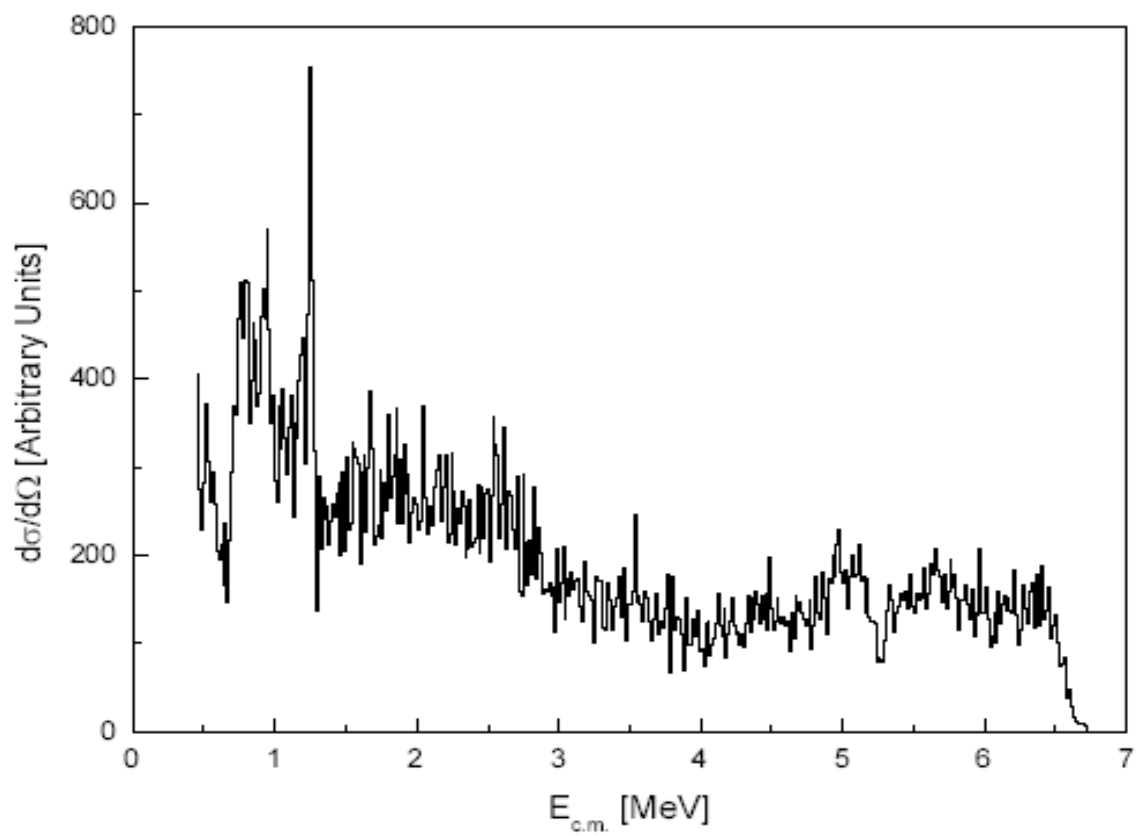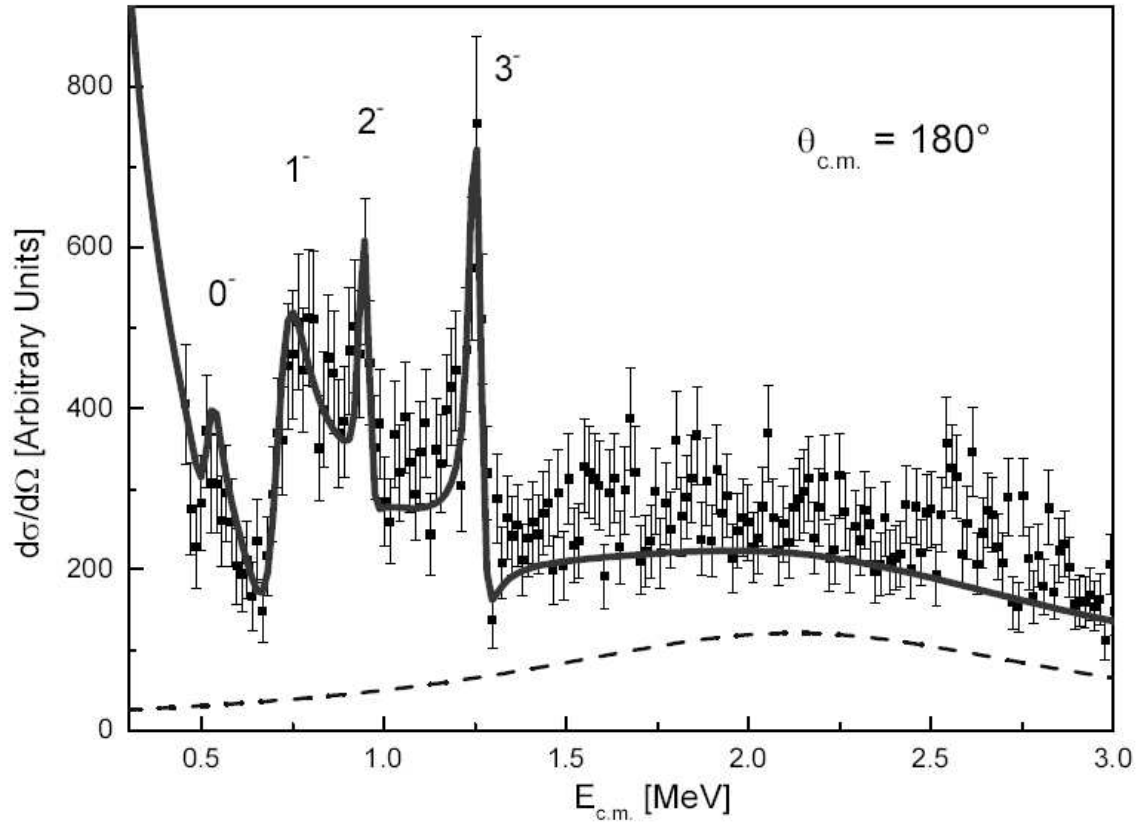| Compilation [Ti93]			^{14}N(^{3}He,n)^{16}F [Za65]		^{14}N(^{3}He,n)^{16}F(p)^{15}O [Ot76]		^{16}O(^{3}He,t)^{16}F [St84]		p(^{15}O,p) [a]		
E_x [MeV ± keV]	J^π	Γ_p[keV]	J^π	Γ_p[keV]	J^π	Γ_p [keV]	J^π	Γ_p[keV]	E_x [b] [MeV ± keV]	J^π	Γ_p[keV]
0	0^-	40 ± 20	0^-	50 ± 30	1^-	39 ± 20	0^-	≈ 25	0	0^-	23.1 ± 2.2
0.193 ± 6	1^-	< 40	2^-	< 40	0^-	96 ± 20	1^-	≈ 100	0.190 ± 20	1^-	91.1 ± 9.9
0.424 ± 5	2^-	40 ± 30	1^-	40 ± 30	≥ 2	24 ± 20	2^-		0.422 ± 19	2^-	3.3 ± 0.6
0.721 ± 4	3^-	< 15	3^-	< 15	≥ 2	24 ± 20	3^-		0.721 ± 17	3^-	14.1 ± 1.7

[a] This work.

[b] The uncertainty primarily comes from the energy calibration (± 15 keV).

Table 6.2 Comparison of ^{16}F experimental results with the isobaric analog states in ^{16}N and with theoretical calculations in the framework of the potential model.

^{16}N			^{16}F			^{16}F Theory			
						Parameter set #1 (a=0.65 fm)	Parameter set #2 (a=0.75 fm)		
Ex [MeV]	J^π	C^2S [a]	E_x [MeV±keV]	J^π	Γ_p[keV][b]	Γ_{sp}[keV]	Γ_{sp} [keV]	C^2S (Exp.)	C^2S (Shift)
0.120	0^-	0.95	0	0^-	23.1 ± 2.2	21.8	22	1.05	0.91
0.397	1^-	0.96	0.190 ± 20	1^-	91.1 ± 9.9	89.5	96	0.95	0.88
0	2^-	0.93	0.422 ± 19	2^-	3.3 ± 0.6	3.6	4.3	0.77	
0.296	3^-	0.87	0.721 ± 17	3^-	14.1 ± 1.7	12.7	15.0	0.94	

[a] OXBASH calculation reported in Ref. [Me96].

[b] This work.

Table 6.3 Woods-Saxon potential model parameters.

	Parameter set #1		Parameter set #2	
	0^-	1^-	0^-	1^-
V	-55.36 MeV	-54.42 MeV	-55.474 MeV	-54.455 MeV
r_o	**1.2 fm**	**1.2 fm**	**1.17 fm**	**1.17 fm**
a	**0.65 fm**	**0.65 fm**	**0.75 fm**	**0.75 fm**
r_c	1.2 fm	1.2 fm	1.2 fm	1.2 fm
V_{so}	7.64 MeV	7.64 MeV	7.64 MeV	7.64 MeV
a_{so}	0.65 fm	0.65 fm	0.65 fm	0.65 fm
$r_{o\,so}$	1.17 fm	1.17 fm	1.17 fm	1.17 fm

CHAPTER 7
Conclusion

7.1 Summary and Conclusion

Nuclear reaction studies with radioactive ion beams has become one of the most compelling research topics in modern nuclear physics. Many accelerator facilities around the world are developing new radioactive ion beams based on the ISOL or PF methods, and proposing advanced technologies to produce higher beam intensities or more exotic beams. The availability of new and improved radioactive ion beams will allow nuclear scientists to explore many unknown nuclei far from the stability, and to work toward a better understanding of the evolution of the universe.

The BEARS facility at Lawrence Berkeley National Laboratory originally provided ^{11}C and ^{14}O radioactive ion beams of high quality. Their beam intensities on target reached up to 2×10^8 pps for ^{11}C and 3×10^4 pps for ^{14}O, respectively. These proton-rich radioactive ion beams have been successfully used to explore new facets of proton-rich unstable nuclei such as ^{12}N and ^{15}F.

In this work, the proton capture reaction on ^{11}C was studied via the indirect d(^{11}C,^{12}N)n transfer reaction using the ANC method. A group at Beijing [Li03] reported the same experiment as we did, but their result was limited since their ^{11}C beam intensity was orders of magnitude lower than was available in our experiment. Using BEARS, our experiment showed that the extracted ANC value is in excellent agreement with theoretical prediction and previous experimental studies. The total effective ^{12}N$\rightarrow$^{11}C+p

ANC is found to be $\left(C_{eff}^{^{12}N}\right)^2 = \left(C_{p_{1/2}}^{^{12}N}\right)^2 + \left(C_{p_{3/2}}^{^{12}N}\right)^2 = 1.83 \pm 0.27\, fm^{-1}$. This study confirmed that the ^{11}C(p,γ) reaction is a key reaction producing CNO nuclei in supermassive low-metallicity stars, bypassing the slow triple alpha process.

Recently, an ^{15}O radioactive ion beam (with an intensity of a few times 10^4 pps on target) was successfully developed at BEARS [Po05], and utilized to study the level widths of ^{16}F. Among the nuclei in the A=16, T=1 isobaric triad, many states in ^{16}N and ^{16}O have been well established, but less has been reported on ^{16}F. Four states of ^{16}F below 1 MeV have been identified experimentally: 0^-, 1^-, 2^-, and 3^- (E_x = 0.0, 0.19, 0.42, and 0.72 MeV, respectively). However, their level widths have remained uncertain for over a decade. Our study found that the 0^- state has a level width of 23.1 $\pm$ 2.2 keV, and that the broader 1^- state has a width of 91.1 $\pm$ 9.9 keV. The level width of the 2^- state is found to be 3.3 $\pm$ 0.6 keV which is much narrower than the compiled value of 40 $\pm$ 30 keV, while 14.1 $\pm$ 1.7 keV for the 3^- state is in good agreement with < 15 keV in Ref. [Ti93]. When compared to shell model theory, all four level widths are seen to be close to the single-particle limit, making them excellent candidates for tests of nuclear reaction theory [Mu05].

7.2 Research Opportunities with BEARS

As mentioned in Chapter 3, $^{7}Be(p,\gamma)^{8}B(\alpha,p)^{11}C(p,\gamma)^{12}N(e^+\nu)^{12}C$ is one of several possible hot pp-chains, producing CNO seed nuclei in supermassive stars. The astrophysical S-factor and the stellar reaction rate of ^{11}C(p,γ) have been experimentally studied with the help of ^{11}C radioactive ion beams at several radioactive ion beam

facilities, including BEARS. However, only a few experimental studies of the $^8B(\alpha,p)^{11}C$ reaction have been reported so far [Re04]. A study of the time-reversed reaction, $^{11}C(p,\alpha)^8B$, will not only verify the importance of this reaction in stellar processes, but provides very useful nuclear reaction data for unstable proton-rich nuclei.

In addition to classical hydrogen burning processes, there are a number of extremely hot, dense astrophysical environments where hydrogen is expected to burn explosively. These include supermassive stars, x-ray bursters, novae, and supernovae. The hot-CNO cycle $^{12}C(p,\gamma)^{13}N(p,\gamma)^{14}O(e^+\nu_e)$ $^{14}N(p,\gamma)^{15}O(e^+\nu_e)^{15}N(p,\alpha)^{12}C$ is one reaction chain, replacing the classic CNO cycle as is shown in Chapter 3 (see Section 3.4). When the stellar temperatures are high enough ($T_9 \geq 0.3$), the β-decay of ^{14}O can be bypassed by the $^{14}O(\alpha,p)^{17}F$ reaction, and the reaction sequence $^{14}O(\alpha,p)^{17}F(p,\gamma)^{18}Ne(e^+\nu_e)^{18}F(p,\alpha)^{15}O$ can increase the energy generation rate and alter the abundances of the CNO nuclides [Ba97]. Hence, a higher intensity ^{14}O radioactive ion beam at BEARS will be a very useful tool to study the $^{14}O(\alpha,p)^{17}F$ reaction.

Furthermore, the reaction sequence $^{14}O(\alpha,p)^{17}F(p,\gamma)^{18}Ne(e^+\nu_e)^{18}F(p,\gamma)^{19}Ne(p,\gamma)^{20}Na$ can provide a path from the hot-CNO cycle into the rapid proton capture process (rp-process) where the energy generation rate is increased by orders of magnitude. In addition to the $^{18}F(p,\gamma)^{19}Ne$ reaction, the other important breakout reactions into the rp-process are identified to be the $^{18}Ne(\alpha,p)^{21}Na$ reaction, and especially, the $^{15}O(\alpha,\gamma)^{19}Ne$ reaction [Wa81]. These breakouts from the hot-CNO cycle into the rp-process can explain how nova explosions can produce the abundances of heavier elements, e.g., Ne, Na, and Al which are seen in nova remnants. Therefore, the newly developed ^{15}O

radioactive ion beam at BEARS also provides a good opportunity to study the $^{15}O(\alpha,\gamma)^{19}Ne$ reaction.

References

[Aj90] F. Ajzenberg-Selove, Nucl. Phys. A506, 1 (1990).

[Ar90] K. T. Artemov et. al., Sov. J. Nucl. Phys. 52, 408 (1990).

[At31] R. D'E. Atkins, Astrophys. J. 73, 250 (1931).

[Ba59] S. Bashkin et. al., Phys. Rev. 114, 1543 (1959).

[Ba97] D. W. Bardayan and M. S. Smith, Phys. Rev. C 56, 1647 (1997).

[Be02] P. F. Bertone et al., Phys. Rev. C 66, 055804 (2002).

[Be03] C. A. Bertulani, Comput. Phys. Commun. 156, 123 (2003).

[Be36] H. A. Bethe and R. F. Bacher, Rev. Mod. Phys. 7, 1 (1936).

[Be39] H. A. Bethe, Phys. Rev. 55, 434 (1939).

[Bl52] J. M. Blatt and L. C. Biedenharn, Rev. Mod. Phys. 24, 258 (1952).

[Bl77] L. D. Blokhintsev, I. Borbely, and E. I. Dolinskii, Sov. J. Part. Nucl. 8, 485 (1977).

[Bo72] W. Bohne et. al., Nucl. Phys. A196, 41 (1972).

[Bo73] W. Bohne et. al., Phys. Lett. B47, 342 (1973).

[Br36] G. Breit and E. P. Wigner, Phys. Rev. 49, 519 (1936).

[Bu57] E. M. Burbidge et. al., Rev. Mod. Phys. 29, 547 (1957).

[Bu88] L. Buchmann, J. M. D'Auria, and P. McCorquodale, Astrophys. J. 324, 953 (1988).

[Ca97] R. F. Casten et al., "White paper: Scientific Opportunities with an Advanced ISOL Facility", Columbus, Ohio, http://www.orau.org/ria (1997).

[Ce96] J. Cerny, in Proceedings of the Exotic Nuclei Symposium, Bodega Bay, CA (1996), D. Moltz, ed., Lawrence Berkeley National Laboratory Report No. LBNL Report-39750 (1996).

[Ce99a] J. Cerny et al., in Proceedings of the 1999 Particle Accelerator Conference (Cat. No. 99CH36366), Piscataway, NJ, 1999, IEEE. Part vol. 1, 533 (1999)..

[Ce99b] J. Cerny, American Institute of Physics Conference Proceedings 518, 3 (2000).

[Da80] W. W. Daehnick et al., Phys. Rev. C 21, 2253 (1980).

[Da84] S. E. Darden et. al., Nucl. Phys. A429, 218 (1984).

[Da05] J. D'Auria, NuPac Meeting, ISOLDE, CERN (2005).

[De62] G. Dearnaley et. al., Phys. Lett. 1, 269 (1962).

[De92] T. Delbar et. al., Nucl. Phys. A542, 263 (1992).

[Eh51] J. B. Ehrman, Phys. Rev. 81, 412 (1951).

[Fa82] A. Fazely et. al., Phys. Rev. C 25, 1760 (1982).

[Fo95] H. T. Fortune, Phys. Rev. C 52, 2261 (1995).

[Fu02] H. Fujita et. al., RCNP Annual Report, 5 (2002).

[Fu86] G. M. Fuller, S. E. Woosley, and T. A. Weaver., Astrophys. J. 307, 675 (1986).

[Ga02] C. A. Gagliardi et al., Eur. Phys. J. A 13, 227 (2002).

[Go04] V. Z. Goldberg et. al., Phys. Rev. C 69, 031302 (2004).

[Gu05] F. Q. Guo et. al., Phys. Rev. C 72, 034312 (2005).

[Ha57] F. B. Hagedorn, Phys. Rev. 108, 735 (1957).

[Ha71] J. D. Harvey, and R. C. Johnson, Phys. Rev. C 3, 636 (1971).

[Im01] N. Imai et al., Nucl. Phys. A688, 281c (2001).

[Ja75] F. James and M. Roos, Comput. Phys. Commun. 10, 343 (1975).

[Jo72] R. C. Johnson and P. J. R. Soper, Nucl. Phys. A182, 619 (1972).

[Jo00] R. Joosten et al., Phys. Rev. Lett. 84, 5066 (2000).

[Ka38] P. L. Kapur and R. E. Peierls, Proc. Roy. Soc. (London) A 166, 277 (1938).

[Ka86] T. Kawamura et al., CYRIC Ann. Rep. 1986, 10 (1986).

[Kr88] K. S. Krane, Introductory Nuclear Physics, John Wiley and Sons, New York, 769 (1988).

[Ku01] S. Kubono, Nucl. Phys. A693, 221 (2001).

[Ku93] P. D. Kunz, computer code DWUCK4, University of Colorado (unpublished), (1993).

[La58] A. M. Lane and R. G. Thomas, Rev. Mod. Phys. 30, 257 (1958).

[Le95] A. Lefebvre et al., Nucl. Phys. A592, 69 (1995).

[Li96] W. Liu et al., Phys. Rev. Lett. 77, 611 (1996).

[Li01] Z. H. Liu et al., Phys. Rev. C 64, 034312 (2001).

[Li03] W. Liu et al., Nucl. Phys. A728, 275 (2003).

[Ma00] K. Markenroth et. al., Phys. Rev. C 62, 034308 (2000).

[Ma97] R. Madey et. al., Phys. Rev. C 56, 3210 (1997).

[Me96] J. Meissner et. al., Phys. Rev. C 53, 977 (1996).

[Mi02] T. Minemura et al., RIKEN Accel. Prog. Rep. A35, (2002).

[Mo66] J. Moss and G. C. Ball, Lawrence Radiation Laboratory Report, UCRL-17124 (1966)

[Mo71] C. E. Moss and A. B. Comiter, Nucl. Phys. A178, 241 (1971).

[Mu01] A. M. Mukhamedzhanov, C. A. Gagliardi and R. E. Tribble, Phys. Rev. C 63, 024612 (2001).

[Mu05] A. M. Mukhamedzhanov and F. M. Nunes, Phys. Rev. C 72, 017602 (2005).

[Mu97] A. M. Mukhamedzhanov et al., Phys. Rev. C 56, 1302 (1997).

[Na77] H. Nann et. al., Phys. Rev. C 16, 1684 (1977).

[No69] J. A. Nolen and J. P. Schiffer, Annu. Rev. Nucl. Sci. 19, 471 (1969).

[Og99] K. Ogawa et. al., Phys. Lett. B464, 157 (1999).

[Oh87] H. Ohnuma et. al., Nucl. Phys. A467, 61 (1987).

[Or82] H. Orihara et. al., Phys. Rev. Lett. 49, 1318 (1982).

[Ot76] T. Otsubo et. al., Nucl. Phys. A259, 452 (1976).

[Pe65] R. H. Pehl and J. Cerny, Phys. Lett. 14, 147 (1965).

[Pe06] K. Peräjärvi et. al., Phys. Rev. C 74, 024306 (2006).

[Po00] J. Powell et. al., Nucl. Instrum. Methods Phys. Res. A 455, 452 (2000).

[Po03] J. Powell et. al., Nucl. Instrum. Methods Phys. Res. B 204, 440 (2003).

[Po06] J. Powell and J. P. O'Neil, Appl. Radiat. Isot. 64, 755 (2006).

[Re04] K. E. Rehm et al., Nucl. Phys. A746, 27 (2004).

[Ri06] http://www.orau.org/ria

[Ro88] C. Rolfs and W. Rodney, Cauldrons in the Cosmos, University of Chicago Press, Chicago (1988).

[Ro98] M. W. Rowe, Ph.D. Thesis, Department of Chemistry, University of California, Berkeley (1998).

[Ru05] C. Ruiz et al., Phys. Rev. C 71, 025802 (2005).

[Sa83] G. R. Satchler, Direct Nuclear Reactions, Oxford University Press, Oxford OX2 6DP (1983).

[St84] W. A. Sterrenburg et. al., Nucl. Phys. A420, 257 (1984).

[Ta03] X. Tang et al., Phys. Rev. C 67, 015804 (2003).

[Te03] T. Teranishi et. al., Phys. Lett. B556, 27 (2003).

[Th51] R. G. Thomas, Phys. Rev. 81, 148 (1951).

[Ti93] D. R. Tilley et. al., Nucl. Phys. A564, 1 (1993).

[Ti03a] N. K. Timofeyuk and S. B. Igamov, Nucl. Phys. A713, 217 (2003).

[Ti03b] N. K. Timofeyuk, R. C. Johnson and A. M. Mukhamedzhanov, Phys. Rev. Lett. 91, 232501 (2003).

[Tu03] M. S. Turner et al., *Connecting Quarks with the Cosmos: Eleven Science Questions for the New Century*", Board on Physics and Astronomy Report, Committee on the Physics of the Universe, National Research Council, The National Academies Press (2003).

[Ve96] J. Vernier, Prog. Part. Nucl. Phys. 37, 435 (1996).

[Vo62] E. Vogt, Rev. Mod. Phys. 34, 723 (1962).

[Wa69] B. A. Watson et al., Phys. Rev. 182, 977 (1969).

[Wa81] R.K. Wallace and S.E. Woosley, Astrophys. J. Suppl. Ser. 45, 389 (1981).

[Wi47] E. P. Wigner and L. Eisenbud, Phys. Rev. 72, 29 (1947).

[Wi89] M. Wiescher et al., Astrophys. J. 343, 352 (1998).

[Xu94] H. M. Xu et al., Phys. Rev. Lett. 73, 2027 (1994).

[Za65] C. D. Zafiratos et. al., Phys. Rev. 137, B1479 (1965).

[Zi03] J. F. Ziegler, The Stopping and Range of Ions in Matter (SRIM-2003), http://www.srim.org.